



RESEARCH ARTICLE

10.1029/2021JA029754

On the Variability of EMIC Waves and the Consequences for the Relativistic Electron Radiation Belt Population

J. P. J. Ross¹ , S. A. Glauert¹ , R. B. Horne¹ , C. E. J. Watt² , and N. P. Meredith¹ 

¹British Antarctic Survey, Natural Environment Research Council, Cambridge, UK, ²Department of Mathematics, Physics, and Electrical Engineering, Northumbria University, Newcastle-upon-Tyne, UK

Key Points:

- Both EMIC waves and hiss waves are necessary to produce the observed decay of 4.2 MeV electrons at $L \leq 3.75$
- The decay of the 2.6 MeV electron flux is largely independent of EMIC activity at $L \leq 3.75$
- EMIC waves largely control the 4.2 MeV electron decay at $L \geq 4.25$ but hiss waves are also important at 2.6 MeV

Correspondence to:

J. P. J. Ross,
johros@bas.ac.uk

Citation:

Ross, J. P. J., Glauert, S. A., Horne, R. B., Watt, C. E. J., & Meredith, N. P. (2021). On the variability of EMIC waves and the consequences for the relativistic electron radiation belt population. *Journal of Geophysical Research: Space Physics*, 126, e2021JA029754. <https://doi.org/10.1029/2021JA029754>

Received 6 JUL 2021
Accepted 5 NOV 2021

Abstract The interactions between electromagnetic ion cyclotron (EMIC) waves and relativistic electrons are influential in diffusing radiation belt electrons into the loss code from which the electrons are lost into the atmosphere. These wave-particle interactions between EMIC waves and electrons with energies of a few MeV or more depend strongly on wave spectra and plasma properties. Here we study the variability in wave spectra and plasma properties as a function of L^* found during Van Allen Probe EMIC observations. These results are used to calculate statistical bounce and drift average diffusion coefficients that include the variation in wave spectra and plasma density as a function of L^* and activity by averaging observation-specific diffusion coefficients. The diffusion coefficients are included in global radiation belt simulations and the effect of the EMIC waves is explored. The distribution in the plasma frequency to electron gyrofrequency ratio decreases to lower values as L^* decreases. As a result, few EMIC waves are able to resonate with 2–3 MeV electrons at $L^* \leq 3.75$ while electrons of the same energy at larger L^* are diffused by EMIC waves in high density regions. In comparison, a sufficient number of EMIC waves are able to resonate with higher energy electrons, ≥ 4.2 MeV, at $L^* \geq 3.25$ to significantly affect the decay in electron flux. EMIC wave parametrisations of electron diffusion by EMIC waves are compared and solar wind dynamic pressure is found to give the best agreement with Van Allen Probe observations.

Plain Language Summary In recent years there has been an increasing number of satellites operating in or traversing the Earth's radiation belts. These belts are composed of charged particles that are largely confined by the Earth's magnetic field, although waves can accelerate and scatter these particles. In the outer belt, electrons can be accelerated up to relativistic energies and pose a threat to satellites. Diffusion-based models are used to simulate the electron population, incorporating the statistical effects of waves on the electrons. Electromagnetic ion cyclotron waves are of particular importance for the relativistic population, effectively scattering them into the atmosphere and removing them from the belts. By following a new approach that captures the variation in the wave-particle interactions, we explore the contributions of electromagnetic ion cyclotron waves to electron loss as functions of electron energy and location in the radiation belts.

1. Introduction

The outer electron radiation belt is highly variable with electron energies reaching up to well over several MeV (Baker et al., 2012). Their behavior is governed by a range of physical processes that when combined give rise to complex spatial and temporal behavior. Whistler mode chorus waves (Horne, Thorne, Glauert, et al., 2005; Horne, Thorne, Shprits, et al., 2005; Glauert & Horne, 2005; Horne et al., 2013; Tsurutani & Smith, 1974; Tsurutani & Smith, 1977) and ultra-low frequency wave (Brautigam & Albert, 2000; Schulz & Lanzerotti, 1974) can accelerate seed population electrons (a few hundreds of keV) up to MeV energies on hour to day timescales (Horne, Thorne, Glauert, et al., 2005). Under quiet conditions, the resulting MeV population is observed to decay on a day to week timescale (Pinto et al., 2019), and therefore, due to its longevity, can pose a significant risk to satellites within the outer radiation belt (Baker et al., 2018).

Theoretical studies have shown that EMIC waves are important for losses of relativistic electrons at $L > 4$ (Kersten et al., 2014; Lyons & Thorne, 1972; Ma et al., 2015; Thorne & Kennel, 1971). Shprits et al. (2016) suggested that EMIC waves were important for electron losses at lower L shells of the slow decaying ultra relativistic storage ring (Baker et al., 2012), although plasmaspheric hiss may also play a significant role (Pinto et al., 2019; Thorne et al., 2013).

©2021. The Authors.

This is an open access article under the terms of the [Creative Commons Attribution License](https://creativecommons.org/licenses/by/4.0/), which permits use, distribution and reproduction in any medium, provided the original work is properly cited.

EMIC wave activity is known to be an activity, L , magnetic local time (MLT), and magnetic latitude dependent. Analysis of CRRES EMIC observations found that occurrence rates in the inner magnetosphere were enhanced in the afternoon sector during geomagnetically disturbed conditions ($AE > 300$ nT) (Meredith et al., 2014), consistent with the theoretical picture of favorable EMIC excitation and growth where anisotropic ring current ions overlap with the high density plasmasphere. Due to the limited duration of the CRRES mission, the prenoon sector had a noticeable gap in data coverage. Analysis using the Van Allen Probes satellites found similar enhanced occurrence rates in the afternoon sector during geomagnetically disturbed conditions, but also a peak during quiet times in the prenoon sector (Saikin et al., 2016; Wang et al., 2016). Day side magnetospheric compressions are also found to be correlated to EMIC wave occurrence rates; enhanced rates are found during high solar wind pressure and positive Dst (Anderson et al., 1992; Usanova et al., 2012). Shabansky orbits can be formed during compression which can result in anisotropic ion populations that generate off equatorial EMIC waves (Shabansky, 1971). While solar wind pressure is low, EMIC waves are observed across all MLT sectors with peak occurrence rates found at prenoon (Saikin et al., 2016). Contrastingly, during high pressure, the peak rates shifts into the afternoon sector (Gamayunov et al., 2020; Saikin et al., 2016).

Statistical studies have found a distinction in density dependence between the EMIC bands. Helium band waves are more prevalent in higher density regions inside the plasmasphere and plasmaspheric drainage plume, whereas hydrogen band waves are largely found in lower density regions outside the plasmasphere (Anderson et al., 1992; Zhang et al., 2016). Such a distinction is consistent with theoretical growth rates (Horne & Thorne, 1994). The range of electron energies and pitch-angles that EMIC waves interact with depends on the cold plasma density and the wave spectrum through the resonance condition (Meredith et al., 2003; Summers et al., 2007). Waves closer to their upper bounding gyrofrequency in high density regions are able to resonate with lower energy and larger pitch-angled electrons. The resonant interactions lead to electron diffusion in pitch-angle, resulting in electron losses from the belts. Therefore, the decay of relativistic and ultrarelativistic electrons in the radiation belts depends on the plasma properties and the wave spectra of the EMIC waves.

The effect of magnetospheric waves on radiation belt electrons is included in global radiation belt models via bounce and drift averaged diffusion coefficients. Recent studies have highlighted the importance of including the variability in plasma properties and wave spectra in radiation belt modeling, for EMIC waves (Ross et al., 2020) as well as whistler-mode waves (Watt et al., 2019, 2021) and Ultra Low-Frequency wave (Thompson et al., 2020). Ross et al. (2020) developed a new approach for calculating electron diffusion coefficients by averaging observation specific diffusion coefficients (each calculated using the wave spectra and plasma density of each individual EMIC wave observation), rather than averaging the wave spectra and density measurements before calculating diffusion coefficients (e.g., Kersten et al. [2014]). This approach, applied to CRRES EMIC observations, significantly improved the agreement between global radiation belt models and Van Allen Probe observations of relativistic and ultra-relativistic electron flux compared to EMIC diffusion models using average wave spectra and plasma density. In particular, higher pitch-angled particles are diffused by the waves, removing a greater proportion of the electron population.

The CRRES EMIC observations, used in Ross et al. (2020), are limited to $L^* \geq 4.0$ due to the magnetometer switching to a lower sensitivity mode at lower L^* (Meredith et al., 2003). However, EMIC waves have been observed by the Van Allen probes at lower L^* (Gamayunov et al., 2020; Qin et al., 2019). Furthermore, the majority of EMIC observations during storms by the CRRES mission were in the storm main phase (Halford et al., 2010), while Saikin et al. (2016) reported more storm-time EMIC observations during the recovery phase during the early years of the Van Allen Probes mission. Additionally, Saikin et al. (2016) noted that EMIC observations observed by the Van Allen Probes have an activity distribution significantly different from those observed by CRRES. The CRRES mission coincided with a considerably more active solar cycle than the Van Allen Probes mission and therefore observed EMIC activity under different solar activity (Wang et al., 2016).

In this paper, we build on the work from Ross et al. (2020) to calculate statistical EMIC diffusion coefficients, by applying a similar approach which includes the variation in wave spectra and plasma properties, by using the more extensive Van Allen Probes data set allowing us to improve the statistics and extend our modeling to lower L^* . The method presented in Ross et al. (2020) for calculating the diffusion coefficients is computationally expensive for extensive wave observation datasets due to the calculation of diffusion coefficients for each observation individually. In this paper, we present an approximate method that reduces the number of calculations necessary while agreeing well with the full calculation. A similar method may be used for modeling electron

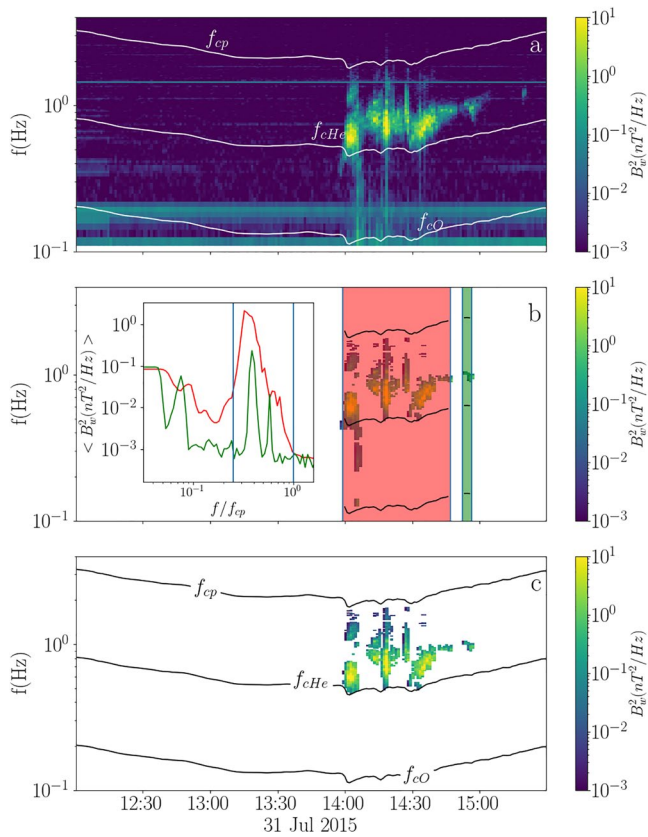


Figure 1. An example electromagnetic ion cyclotron (EMIC) observation on 31 July 2015 by Van Allen Probe A. Panel (a) shows the power spectrum with the hydrogen, helium, and oxygen gyrofrequencies plotted in white. The power over the frequency-dependent threshold is shown in panel (b), where 2 events are identified and illustrated by the red and green shading. The average power spectra over the duration of the events, used in the events validation, are shown in the inset to panel (b). Panel (c) shows the result of the identification when the wave power in the helium band has been removed as it has not been classified as EMIC.

diffusion by other wave modes in the radiation belts. These EMIC diffusion coefficients are then included in global radiation belt simulations to explore the effects of EMIC waves on ultrarelativistic electrons.

Our identification and analysis of the Van Allen Probes EMIC wave observations is presented in Section 2, with a focus toward the variation in wave spectra and plasma density and the implication for resonant energies. In Section 3 we calculate statistical bounce and drift averaged EMIC diffusion coefficients by averaging observation-specific diffusion coefficients parameterized by P_{dyn} , Dst and Kp . In Section 4 we include these matrices into a global radiation belt model to assess the importance of EMIC waves and to compare the EMIC parameterizations. The results are discussed in Section 5 and our conclusions are presented in Section 6.

2. EMIC Wave Observations

In this study, we use data from the Van Allen Probe satellites that were launched on the 30 August 2012 into a near-equatorial (10° inclination) elliptical orbit with a perigee of $1.1R_E$ and apogee of $5.8R_E$ (Mauk et al., 2013). For the EMIC wave observations, we use the 64 Hz magnetometer data from the Electric and Magnetic Field Instrument Suite and Integrated Science (EMFISIS) between 11 September 2012 and 13 October 2019 (Kletzing et al., 2013). We do not use data from the Van Allen Probe B as we cannot reliably determine if the two sets of measurements are independent; the same EMIC waves observed by one instrument may also be observed by the other due to the temporal and spatial coherence of the waves (Blum et al., 2017). Additionally, the magnetometer data from Van Allen Probe A is generally less noisy than that from B, and therefore EMIC wave identification is more reliable (Wang et al., 2015).

2.1. Data Analysis and Extraction

The wave spectra are calculated using the magnetic field measurements rotated into a mean-field-aligned coordinate system where the coordinate transformation is performed based on the method from Jun et al. (2019), using a 32 s moving average for the background field. The mean-field-aligned orthonormal basis is defined by $\hat{e}_z = \mathbf{B}/|\mathbf{B}|$, the y-component is in the direction

$\mathbf{B} \times \mathbf{r}$ and \hat{e}_x completes the right hand system via $\hat{e}_x = \hat{e}_y \times \hat{e}_z$. We apply for a 3rd order Butterworth bandpass filter with a lower cut-off of 0.1 Hz and an upper cut-off of 10 Hz along each component (Wang et al., 2015). The power spectral density (PSD) of the waves is calculated using a fast Fourier transform applied to each magnetic field component with a Hanning time window of 64s with a stepsize of 16s. The wave properties are then calculated from the co-variance matrix in the frequency domain $J_{ij}(f) = X_i(f)X_j^*(f)$, where $X_i(f)$ are the Fourier transforms of the magnetic field components, following Means (1972). The wave properties are then averaged over 4 windows, giving a 64s measurement cadence.

At $L^* < 3$, the proton gyrofrequency increases to ≥ 10 Hz which becomes comparable to the Nyquist frequency of the 64 Hz magnetometer on EMFISIS. We, therefore, limit our analysis to $L^* > 3$, otherwise, we would be artificially restricting EMIC wave detections to frequencies significantly lower than the proton gyrofrequency at lower L^* (Wang et al., 2015).

Wave features are extracted by the following algorithm based on Bortnik et al. (2007). In order to remove ambient noise, the rolling 3 min average PSD must exceed 10 times the daily average (Usanova et al., 2012), and therefore long lasting background features, likely resulting from the satellite itself, are excluded. For example, the narrow band wave power at ~ 1.5 Hz (horizontal line in Figure 1a) does not satisfy this criterion and is therefore excluded. Occasionally, short-duration bursts of wave power occur which do not correspond to EMIC activity (Usanova et al., 2012), we exclude these by imposing the constraint that wave features must persist for a minimum of 5 min.

In order to capture most of the wave power of bursty events, shorter duration bursts in wave power that exceeds the threshold that is separated by less than 5 min from an existing feature are identified as the same feature (Wang et al., 2015), as illustrated in Figure 1b. As we require simultaneous density and spectral measurements for our diffusion coefficient calculations, we excluded observations when there is no f_{pe}/f_{ce} provided in the Level 4 EM-FISIS data (Kurth et al., 2015) leaving ~60% of the Van Allen Probe A data which we analyze.

After performing the feature extraction, we verify that the features are EMIC waves and remove broad band signals and magnetosonic waves (Anderson & Hamilton, 1993). For this, we use a combination of visual identification and supervised machine learning. First, we visually validate the features during 2013 and 2014 and label the features appropriately as EMIC or non-EMIC, for each band separately. For each feature, we then average the power spectral density over time on a frequency grid normalized by the proton gyrofrequency (see the subplot in Figure 1b). A Random Forest is then trained and tested on the average power spectral density profiles and validation labels from the visually inspected 2014 and 2013 observations, respectively. The prediction accuracy is ~95%, where the differences in classification are low amplitude EMIC waves that are excluded by the Random Forest. The trained Random Forest is then applied to the remaining dataset of candidate features to identify the EMIC waves. An example of EMIC wave activity identified by the Random Forest is shown Figure 1c. The broadband wave power below the helium gyrofrequency that is picked out by our extraction algorithm is classified as non-EMIC by the Random Forest method and therefore rejected from the EMIC dataset.

To aid our analysis of the EMIC wave spectra and to only select the most intense harmonic within the band, we fit a Gaussian distribution to the power spectral density at each instance in time to each EMIC band. The corresponding upper and low cut-offs are determined by the highest and lowest frequency within the band that was identified as being above the threshold. Note that each EMIC wave feature will be made up of multiple line spectra at different instances in time, resulting in multiple fitted distributions for a given event, each representing 64 s of the EMIC wave, rather than averaging over the duration of the duration as is often done. For each of the spectral profiles, we retain the central Gaussian frequency, f_m , the Gaussian width, and the upper and lower cut-offs. The wave intensity, $B_w^2(nT^2)$, is then calculated by integrating the Gaussian distribution between the the cut-offs. Additionally, we retain f_{pe}/f_{ce} , MLT, the magnetic latitude and L^* along with solar wind parameters and geomagnetic indices from the OMNI web. For consistency with our previous diffusion coefficient calculations, we calculate L^* using OP77Q (W. P. Olson & Pfitzer, 1977).

2.2. Activity and Spatial Dependence

The distribution of EMIC waves depends on the solar and geomagnetic activity as well as the spatial location in the radiation belts. We, therefore, perform a statistical analysis of the EMIC wave activity which we can use to interpret later results. For brevity, we focus on the distributions in MLT and L^* parameterized by solar wind pressure, P_{dyn} , as similar statistical studies have been performed before, for example, see Chen et al. (2019), Jun et al. (2019), Saikin et al. (2016).

During the weak solar activity, $P_{dyn} \leq 2$ nPa shown in Figure 2 a and b, the occurrence rates of hydrogen and helium band EMIC waves peak at $\lesssim 1\%$ just prior to noon. In comparison, the helium band waves have a broader distribution in MLT with slightly enhanced rates in the afternoon sector and predawn. The occurrence rate increases with increasing L^* for both bands. The MLT and L^* dependence of the average wave intensity, Figures 3a and 3b are well correlated with the occurrence EMIC rate.

At high solar wind activity, $P_{dyn} > 5$ nPa shown in Figures 2e and 2f, the EMIC occurrence rates are significantly increased from the levels found during weak solar activity. Again the rates increase with L^* and by $L^* \sim 5$, the occurrence rates reach 5%–10%, a factor of ~10 increase compared to during the weak solar activity. There are enhanced hydrogen band EMIC occurrence rates at $L^* \geq 5$ over a broad range of MLT, from 2–19. Contrastingly, the wave intensity is peaked in the afternoon sector, Figure 3e. The hydrogen band waves outside of the afternoon sector are typically low amplitude, resulting in a lower average power spectral intensity. On the other hand, the helium band waves are largely found between 10 and 20 MLT, with few observations in the predawn sector. Enhanced EMIC wave activity on the dusk side is consistent with previous statistical studies (Meredith et al., 2014; Saikin et al., 2015) and self-consistent global models of EMIC wave excitation (Jordanova et al., 2008).

Before we calculate drift and bounce averaged diffusion coefficients, we need to understand the L^* and activity dependence. We therefore average observations from each MLT and bin by L^* , and P_{dyn} , Kp , and Dst in turn.

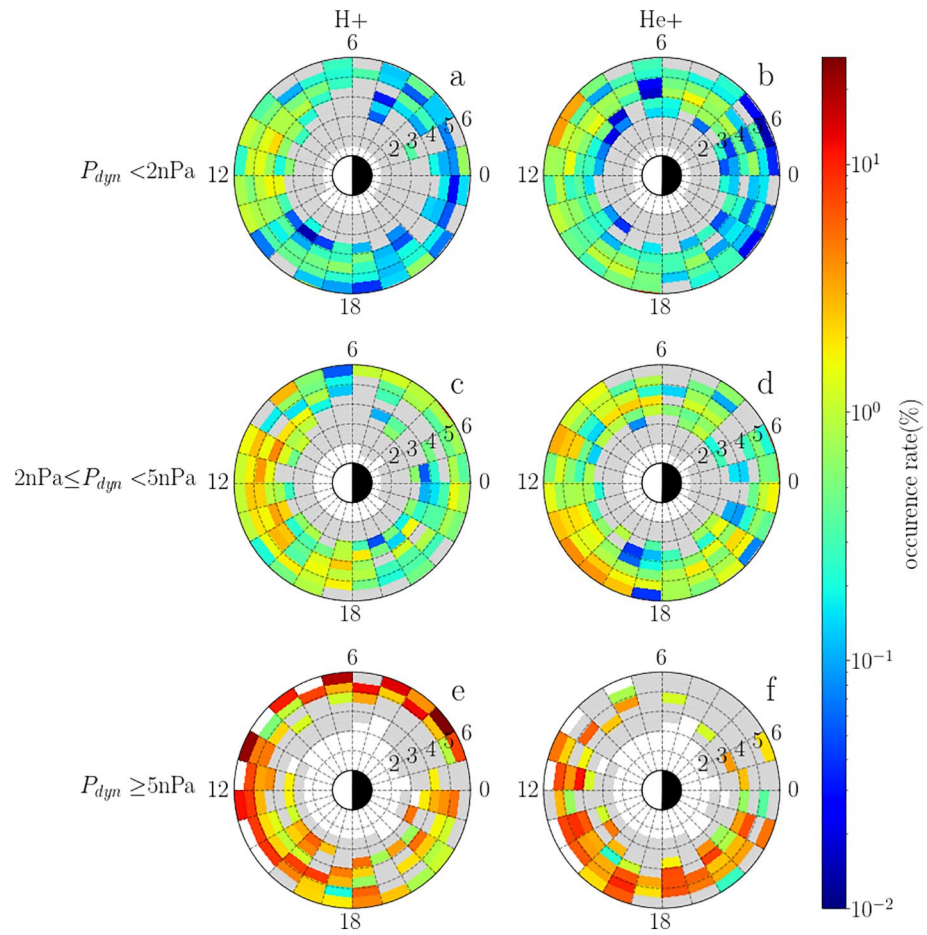


Figure 2. Occurrence rates for hydrogen and helium band electromagnetic ion cyclotron waves as a function of magnetic local time and L^* for $P_{dyn} < 2$ nPa, $2 \text{ nPa} \leq P_{dyn} < 5$ nPa and $P_{dyn} \geq 5$ nPa. The gray shading indicates that there are at least 2 hr of observations in a bin.

Figures 4a and 4b show that the MLT averaged occurrence rates increase with P_{dyn} for both hydrogen and helium band EMIC waves. The strongest P_{dyn} dependence is found at larger L^* , with the occurrence rate reaching over 4% for hydrogen and over 3% for helium at $L^* = 5.25$. Contrastingly, while $P_{dyn} < 2$ nPa, the occurrence rates at all L^* are less than 0.5% for each band. However, there are more EMIC wave observations during these quiet times than during high solar wind pressure, as shown in Figures 4c and 4d, despite the low occurrence rate as a result of longer satellite dwell times. The total duration of the EMIC wave observations increases with L^* until $L^* = 5.25$. The decrease at $L^* = 5.75$ is due to lower dwell times and that the low-frequency limit of the Butterworth band pass filter approaches f_{cHe} in the weaker magnetic field making identification of helium band EMIC waves more difficult. The average EMIC wave intensity for both bands, including times with EMIC activity and without EMIC waves identified that is, the average wave intensity over all time in the bin, increases significantly with P_{dyn} even at low L^* with $\langle B_w^2(nT^2) \rangle$ for helium bands waves reaching $> 10^{-2} nT^2$ at $L^* = 3.75$ and $P_{dyn} \geq 5$ nPa, compared to $\sim 10^{-4} nT^2$ when $P_{dyn} < 1$ nPa. For our activity binning for our diffusion coefficient calculations, we want the binning to reflect the changes in the EMIC wave occurrence and wave intensity while retaining good statistical coverage. At $L^* = 4.75$ and 5.25 , the occurrence rate increases substantially between the $4 \text{ nPa} \leq P_{dyn} < 5 \text{ nPa}$ and $P_{dyn} \geq 5 \text{ nPa}$ bins, and therefore, for our diffusion coefficient calculations, we choose 5 nPa as the lower threshold for as our largest P_{dyn} bin. The minimum total observation duration, with or without EMIC activity, when $P_{dyn} > 5$ nPa within each L^* and P_{dyn} bin is 72 hr, although the duration of the observed EMIC activity at $L^* = 3.25$ within this bin is low. For the lower bins, we adopt $P_{dyn} < 1$ nPa, $1 \text{ nPa} \leq P_{dyn} < 2$, and $2 \text{ nPa} \leq P_{dyn} < 5$ nPa, each of which has greater than 650 hr of observations.

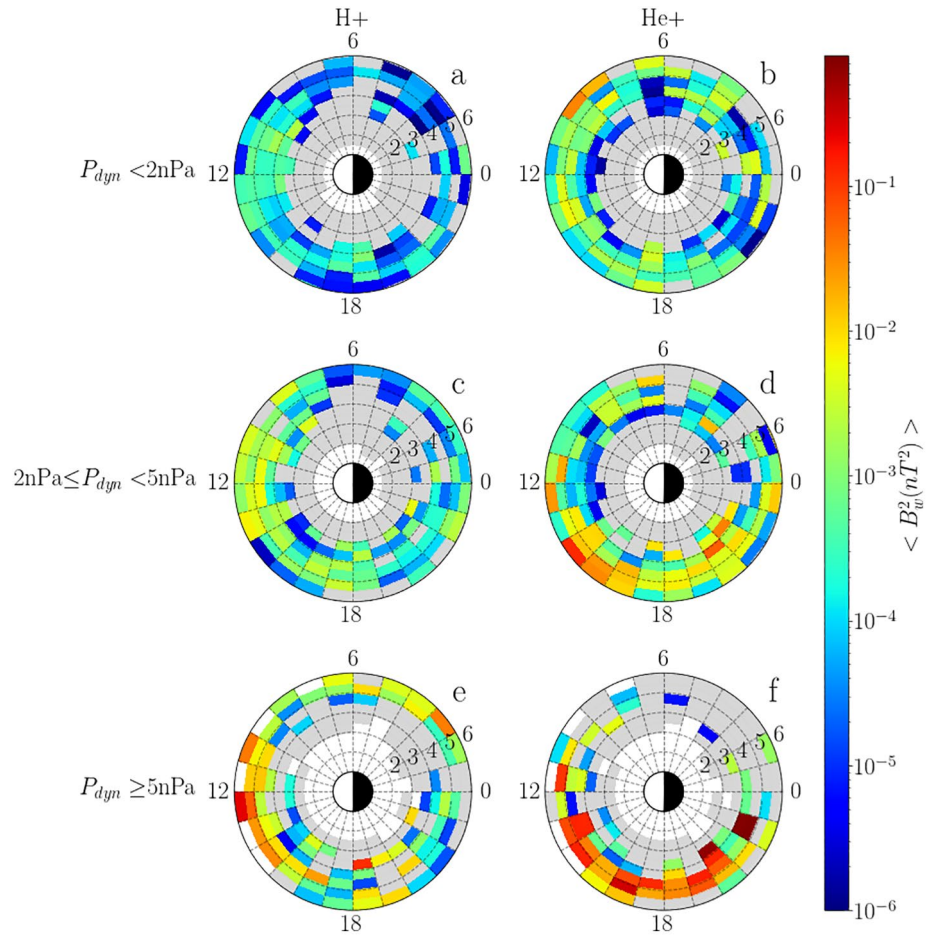


Figure 3. Average wave intensity for hydrogen and helium band electromagnetic ion cyclotron waves as a function of magnetic local time and L^* for $P_{dyn} < 2 \text{ nPa}$, $2 \text{ nPa} \leq P_{dyn} < 5 \text{ nPa}$ and $P_{dyn} \geq 5 \text{ nPa}$. The gray shading indicates that there are at least 2 hr of observations in a bin.

Figures 5a and 5b show that the occurrence rates of both hydrogen and helium band EMIC waves increase with Kp at all L^* between $Kp < 1$ and $4 \leq Kp < 5$. The dependence is again strongest at larger L^* , particularly for helium band EMIC, with occurrence rates reaching $\sim 4\%$ at $L^* \geq 4.75$ during active conditions. The average wave power of both bands shows a strong dependence on Kp at all L^* and therefore we take $Kp < 2$, $2 \leq Kp < 4$ and $Kp > 4$ as our bins for diffusion coefficient modeling. At $Kp > 4$, each L^* bin has greater than 63 hr of observations while the lower Kp bins have at least ~ 630 hr.

Finally, Figures 6a and 6b show that the highest occurrence rates are found when Dst decreases at all L^* . At $L^* = 3.25$, the majority of the EMIC wave observations are at $\text{Dst} < -20 \text{ nT}$ with few at higher values of Dst, Figures 6c and 6d. However, at $L^* \geq 4.25$, the dependence of EMIC occurrence rates of Dst is significantly weaker, particularly at larger L^* . The average wave intensity also increases with decreasing Dst at all L^* s although the dependence is again stronger at lower L^* . We note that there is a substantial difference between the strength of the geomagnetic storms within the $-200 \text{ nT} \leq \text{Dst} < -50 \text{ nT}$ and $-50 \text{ nT} \leq \text{Dst} < -20 \text{ nT}$ bins, however the average wave intensity within these bins are very similar, and therefore we combine them. We discuss this further in the discussion. Our activity binning is then $\text{Dst} < -20 \text{ nT}$, $-20 \text{ nT} \leq \text{Dst} < 5 \text{ nT}$, and $\text{Dst} > 5 \text{ nT}$, with each bin having more than 350 hr of observations.

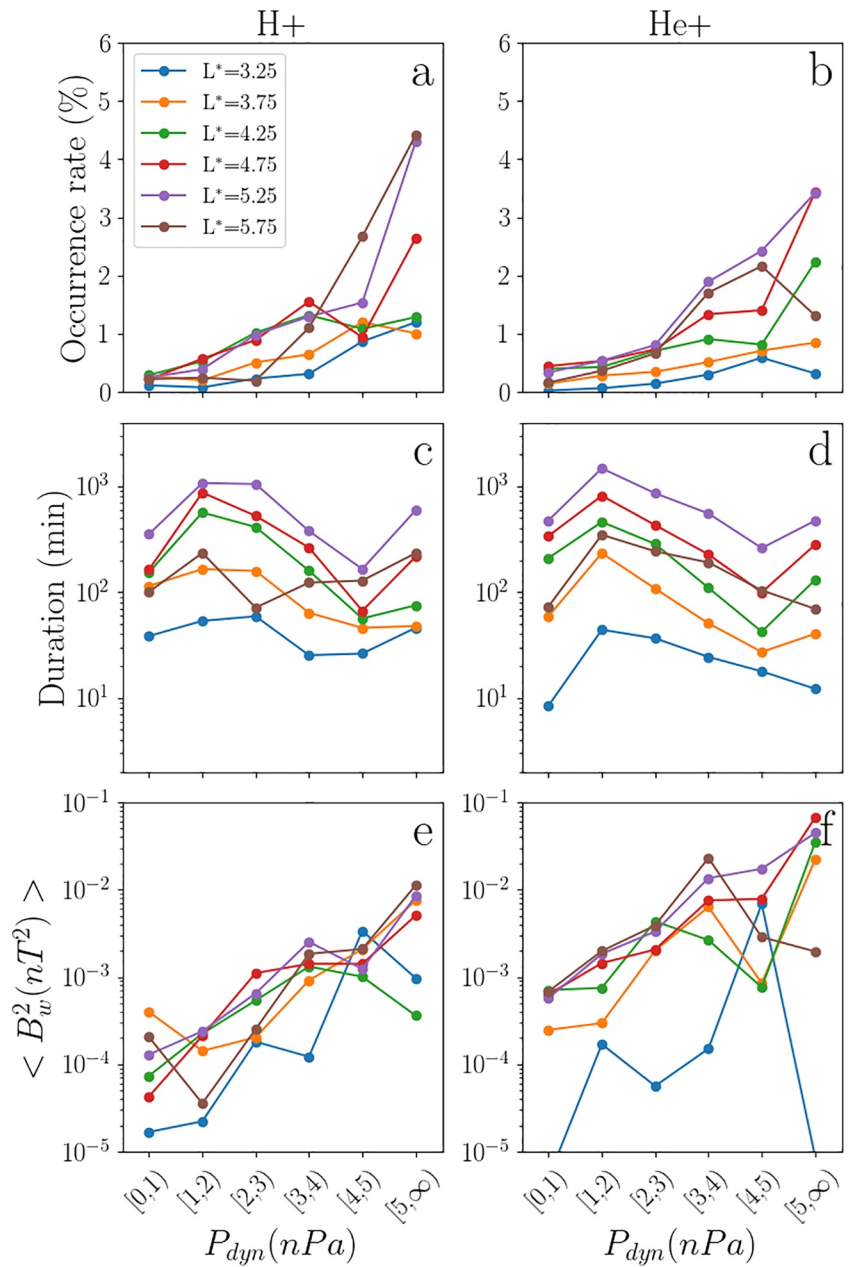


Figure 4. Panels (a) and (b) show the average occurrence rate for hydrogen and helium band electromagnetic ion cyclotron (EMIC) waves as a function of P_{dyn} with the L^* bin indicated by the line plot color. Panels (c) and (d) show the corresponding EMIC duration within the P_{dyn} and L^* bins. The average wave intensities are given in (e) and (f). The round brackets indicate strict inequality while the square brackets allow for equality for example, (0, 1) corresponds to $0 \text{ nPa} \leq P_{dyn} < 1 \text{ nPa}$.

2.3. Variability in Spectral and Plasma Properties

In this section, we discuss the variability of the EMIC wave spectra and plasma density as these two properties strongly influence the wave-particle interactions. For this, we map the observations to the equator, as equatorial values are necessary for the diffusion coefficient calculations, and diffusion by EMIC waves is dominated by low latitude wave-particle interactions (see Section 3.2). For the mapping we assume a dipole magnetic field and that the wave power and plasma density remain constant along the field. In an average sense, close to the magnetic equator ($IMLATI < 20^\circ$) the plasma density deviates little from the equatorial value, for example, see Ozhogin et al. (2012) Figure 9.

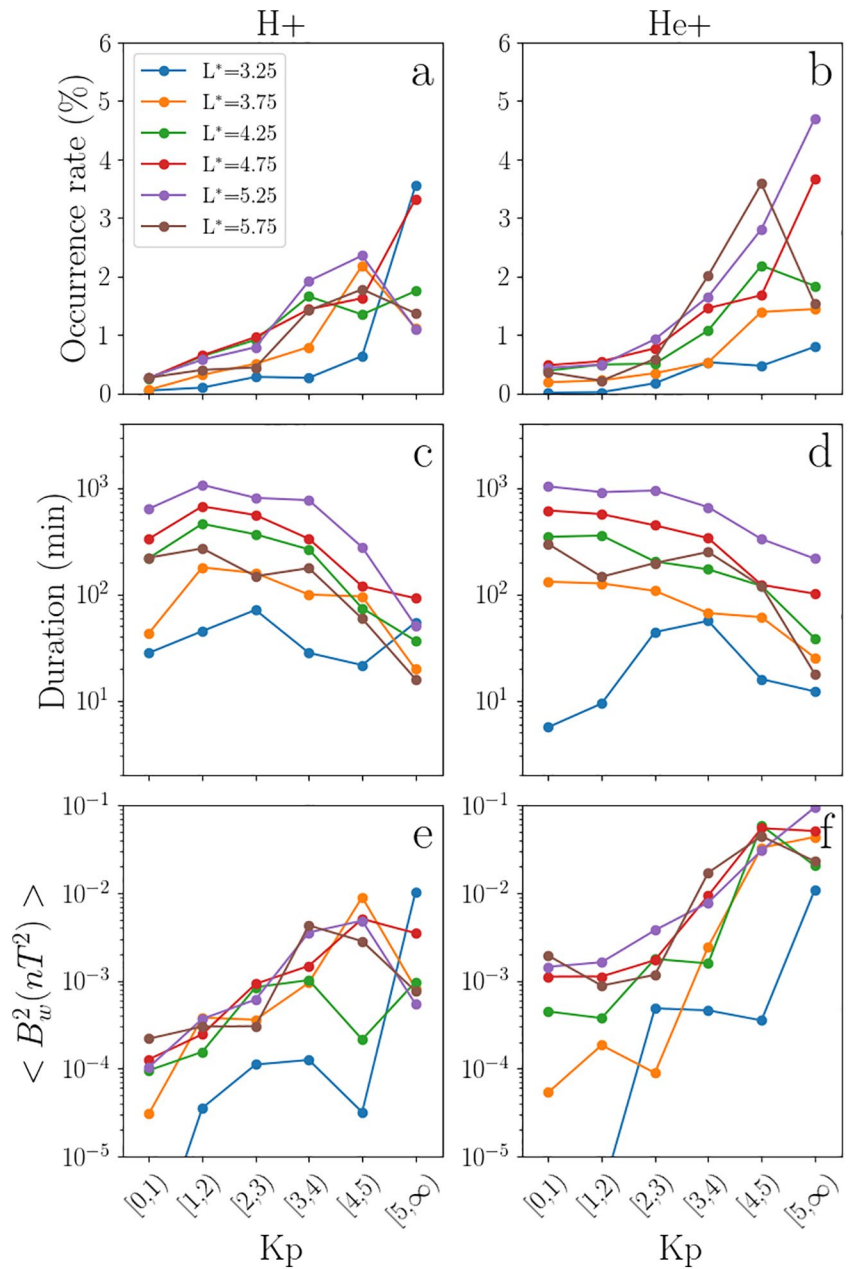


Figure 5. Panels (a) and (b) show the average occurrence rate for hydrogen and helium band electromagnetic ion cyclotron (EMIC) waves as a function of Kp with the L^* bin indicated by the line plot color. Panels (c) and (d) show the corresponding EMIC duration within the Kp and L^* bins. The average wave intensities are given in (e) and (f). The same notation for the brackets is used as in Figure 4.

As mentioned above, the resonance between EMIC waves and electrons is sensitive to the wave spectrum and f_{pe}/f_{ce} . This can be seen in Figure 7, when the wave frequency approaches the upper bounding gyrofrequency of the band, the minimum resonant energy, E_{\min} , significantly decreases. Similarly, in high-density regions where f_{pe}/f_{ce} is large, E_{\min} is also decreased. Therefore, knowledge of how the wave spectra and f_{pe}/f_{ce} relate to each other and vary with L^* is necessary for accurately modeling wave-particle interactions.

In order to represent the wave spectra, we can consider the Gaussian central frequency, f_m , as this gives an indication of the frequency at which the EMIC wave power is centered. The distribution of f_m/f_{cp}^{eq} remained fairly constant between $L^* = 3.2$ and 5.7 for both hydrogen and helium band waves, Figures 8a and 8b, with little variation in average (crosses) and the 20% and 80% percentiles (black lines). There is a second small population

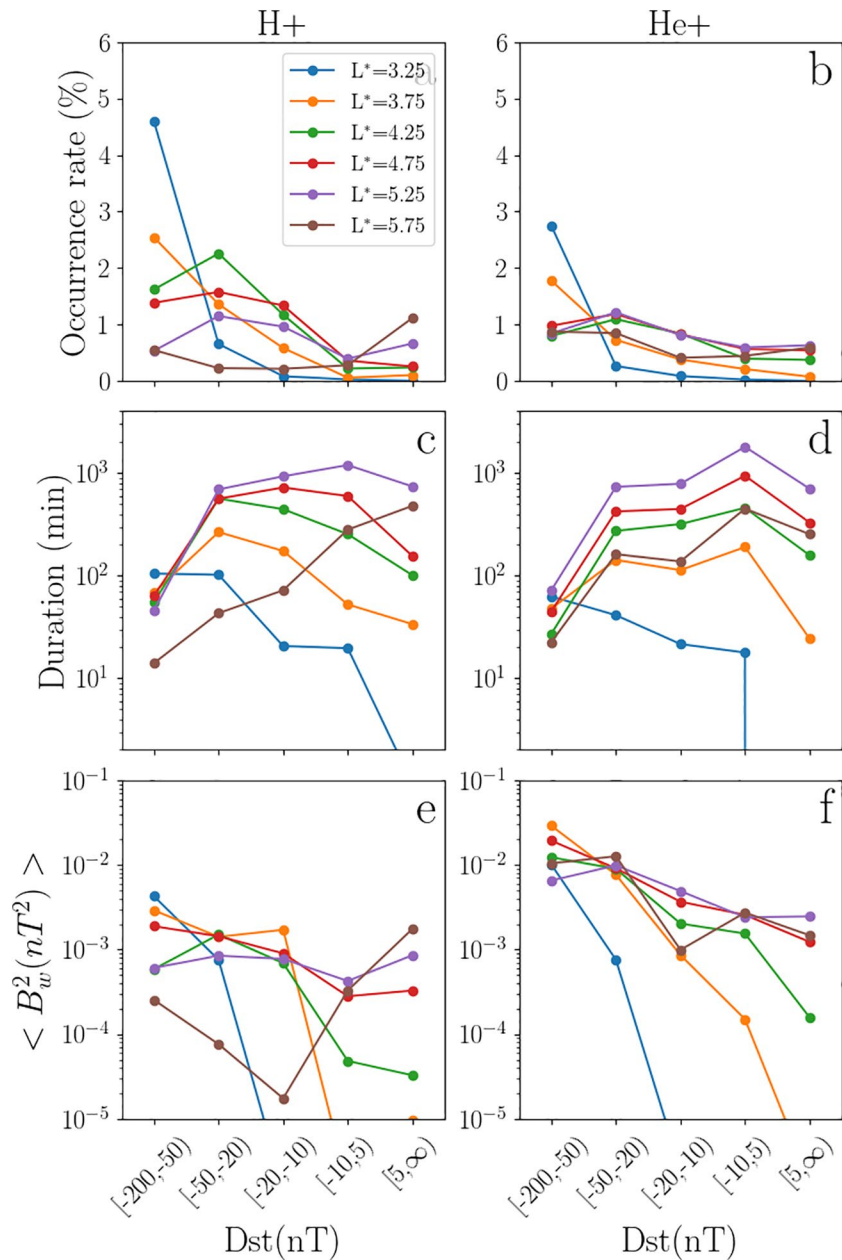


Figure 6. Panels (a) and (b) show the average occurrence rate for hydrogen and helium band electromagnetic ion cyclotron (EMIC) waves as a function of Dst with the L^* bin indicated by the line plot color. Panels (c) and (d) show the corresponding EMIC duration within the Dst and L^* bins. The average wave intensities are given in (e) and (f). The same notation for the brackets is used as in Figure 4.

of hydrogen band EMIC waves close to the proton gyrofrequency with $f_m/f_{cp}^{eq} > 0.9$ found at $L^* \geq 4.0$ (Teng et al., 2019). At $L^* \leq 4$, the Butterworth upper cut-off frequency may be limiting the hydrogen distribution at high frequencies (red line), however, Teng et al. (2019) found that the number of high frequency EMIC waves decrease with decreasing L^* and few were found at $L^* \leq 3.5$. The distribution of f_m/f_{cp}^{eq} for hydrogen band EMIC waves is peaked at ~ 0.42 , consistent with the CRRES EMIC observations (Kersten et al., 2014; Meredith et al., 2014), with the 80% of observations with $f_m/f_{cp}^{eq} < 0.45$. The helium band waves have a broader distribution in f_m relative to its gyrofrequency with a significant number of observations close to the helium frequency. For instance, 20% of helium EMIC waves have f_m above $\sim 0.75f_{cHe}$ and $\sim 20\%$ have f_m less than $\sim 0.5f_{cHe}$, while the average value is $\sim 0.65f_{cHe}$, allowing helium band waves to resonate with a broad range of electron energies and pitch-angles.

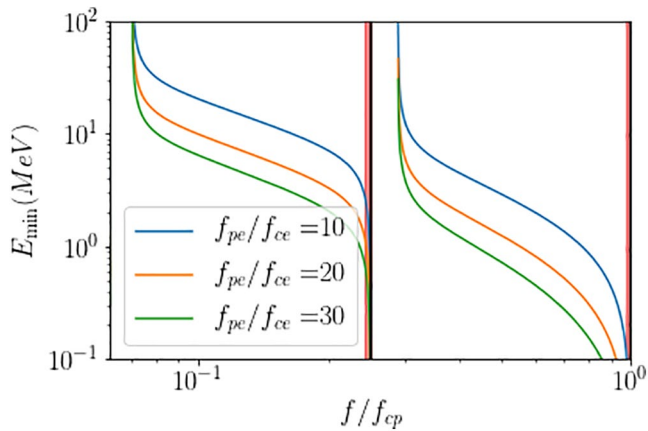


Figure 7. Profiles of the minimum resonant energy assuming field-aligned waves for various f_{pe}/f_{ce} and ion composition of 94% hydrogen, 5% helium, and 1% oxygen. The red shaded regions give the prohibited frequency ranges used in the diffusion coefficient calculation, specified by f_{up} .

For both bands, the average f_{pe}/f_{ce}^{eq} , shown by the crosses in Figures 9a and 9b, increases with L^* although the increase is much shallower for hydrogen band waves. Between the two wave bands, there is a clear distinction in distribution in f_{pe}/f_{ce}^{eq} . Helium band EMIC waves are found in predominantly higher density regions, such as a plasmasphere and plasmaspheric plumes, while hydrogen band EMIC waves are largely associated with lower density regions, such as the plasma trough, where the 80th percentile of hydrogen band densities is close to the 20th percentile of helium band densities at $L^* \geq 4.0$ (black lines) (Anderson et al., 1992; Horne & Thorne, 1994; Zhang et al., 2016). However, there is significant variation in f_{pe}/f_{ce}^{eq} at fixed L^* with the highest obtained f_{pe}/f_{ce}^{eq} increasing with L^* . As a result of the lower f_{pe}/f_{ce}^{eq} values found at low L^* , these EMIC waves will typically resonate with higher energies than those at high L^* , unless there is wave power very close to the upper bounding gyrofrequency, Figure 7. Note that while an electron drifts around the Earth, at fixed L^* , it may interact with EMIC waves in a wide range in plasma densities as it changes MLT, this variation must be captured when calculating drift averaged diffusion coefficients.

We have over-plotted the L dependent density models from Sheeley et al. (2001) (red dotted line) and Ozhogin et al. (2012) (blue dotted line)

in Figure 9, calculated assuming a dipole magnetic field and so $L = L^*$. At $L^* \geq 4.0$, the L^* dependent average f_{pe}/f_{ce}^{eq} found in the helium band EMIC observations exceeds both plasmaspheric density models and, by $L^* \sim 5.0$, 80% of the observations have higher densities than these models. At $L^* \leq 3.6$, the average f_{pe}/f_{ce}^{eq} for a helium band observation drops below the plasmaspheric density models and the majority of the observations are at lower densities. For hydrogen band EMIC waves, the L^* dependent average f_{pe}/f_{ce}^{eq} lies between the plasmaspheric models and the Sheeley et al. (2001) plasma trough model (red dash-dot line). Approximately 20% of observations are at lower densities than the Sheeley et al. (2001) plasma trough model and $\sim 20\%$ of observations exceed the plasmasphere models. For comparison we have plotted the distributions of f_{pe}/f_{ce}^{eq} at all times, including times with EMIC activity and without, in Figure 9c. The average over all times lies close to the statistical plasmasphere models of Sheeley et al. (2001) and Ozhogin et al. (2012).

Finally, we show the distribution in f_m/f_{cp}^{eq} as a function of f_{pe}/f_{ce}^{eq} in Figure 10. From this combination of parameters, assuming an ion composition of 94% hydrogen, 5% helium, and 1% oxygen (Kersten et al., 2014) and that the EMIC waves are field-aligned, we can calculate the minimum resonant energies which are shown by the black contours over-plotted in Figure 10. Note that the wave power of the waves extends to higher and lower frequencies as the wave spectra have a nonzero width. There are a considerable number of both hydrogen and helium band waves that can resonate with $\lesssim 3$ MeV electrons but significantly fewer that can resonate with $\lesssim 1$ MeV electrons, and these are largely hydrogen band waves close the proton gyrofrequency, for instance, the high frequency

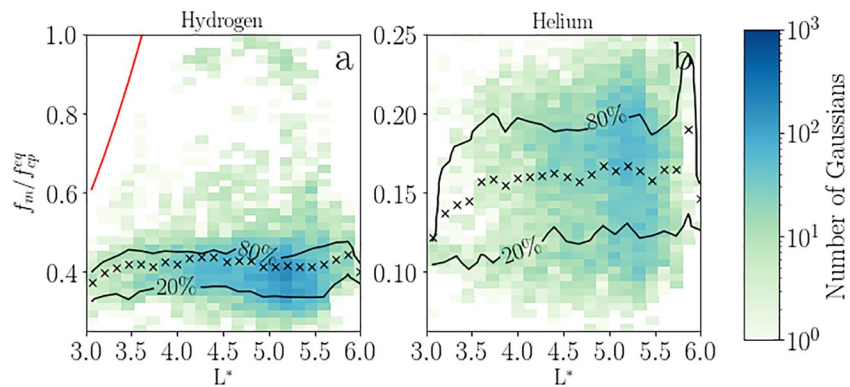


Figure 8. The distribution of (a) Hydrogen band and (b) Helium band electromagnetic ion cyclotron waves observations in terms of L^* and f_m/f_{cp}^{eq} , where the color indicates the number of observations in the corresponding L^* and frequency bin. The back crosses indicate the mean f_{pe}/f_{ce}^{eq} at a given L^* , while the black solid lines are the 20% and 80% percentiles. The red line indicates the equatorial cut-off frequency of the Butterworth band pass filter.

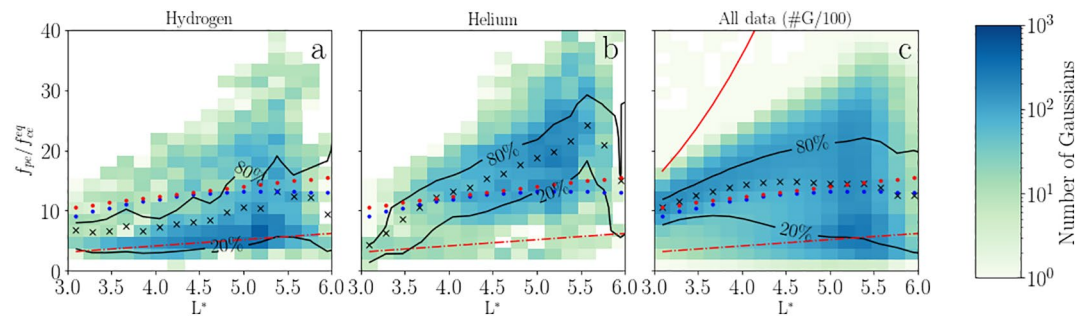


Figure 9. The distribution of (a) Hydrogen band, (b) Helium band electromagnetic ion cyclotron (EMIC) waves in terms of L^* and f_{pe}/f_{ce}^{eq} . Panel (c) gives the distribution of f_{pe}/f_{ce}^{eq} for all observations, including EMIC and non-EMIC times, the number of observations has been divided by 100 to lie on the same color scale. The back crosses indicate the mean f_{pe}/f_{ce}^{eq} at a given L^* , while the black solid lines are the 20% and 80% percentiles. For comparison, the blue dotted line and red dotted lines are the f_{pe}/f_{ce}^{eq} values calculated using the Ozhogin et al. (2012) plasmaspheric electron density model, Sheeley et al. (2001) plasmaspheric electron density model, Sheeley et al. (2001) plasma trough model is given by the red dash-dot line. The maximum value of f_{pe}/f_{ce}^{eq} that can be derived by the electric and magnetic field instrument suite and integrated science data using the highest frequency bin of the HRF receiver and the upper hybrid resonance is shown by the solid red line.

hydrogen population (Teng et al., 2019). Note that the cold plasma dispersion relation, used here, breaks down close to the gyrofrequency when the refractive index tends to infinity. As a result, the lowest resonant energies (< 1 MeV) are likely to be underestimated by this approximation.

3. EMIC Diffusion Coefficients

In order to include electron diffusion by EMIC waves in global radiation belt models, we calculate statistical drift and bounce averaged diffusion coefficients, $\langle D_{\alpha\alpha} \rangle^D$, using the PADIE code (Glauert & Horne, 2005). PADIE solves the cold plasma dispersion relation and uses quasi-linear theory to calculate the diffusion coefficients. In this work, we use a modified version of the PADIE code that takes an arbitrary wave power spectral density as an input rather than Gaussian inputs. We calculate statistical bounce averaged diffusion coefficients for both hydrogen and helium band EMIC waves by averaging observation-specific diffusion coefficients (Ross et al., 2020).

3.1. Calculation

The orbit of the Van Allen Probe satellites is inclined with respect to the geomagnetic equator, we, therefore, map each of the EMIC observations to the magnetic equator assuming a dipole, and that the number density and magnetic power spectra do not change with latitude along the magnetic field line. The average EMIC wave power observed by the Van Allen probes is approximately constant with latitude for absolute magnetic latitudes of $\leq 17^\circ$. We use the superscript *eq* to identify equatorial values and prevent ambiguity. We restrict our diffusion coefficient calculations to magnetic latitudes less than 20° assuming that the EMIC wave spectral profile does not vary with geomagnetic latitude. Summers et al. (2007) found that electron diffusion, by EMIC waves, at the loss cone is dominated by waves at $|\lambda_{mag}| < 20^\circ$: diffusion at larger equatorial pitch angles is restricted close to the magnetic equator. By neglecting wave power at higher magnetic latitudes we underestimate diffusion at high energies typically above 10 MeV. We discuss this further below in Section 3.2. For our nominal ion abundances, we use 94% hydrogen, 5% helium, and 1% oxygen following Kersten et al. (2014). For the local upper cut-off, f_{up} , we take a value of 0.97 following Ross et al. (2020) to avoid warm plasma effects close to the upper bounding gyrofrequency

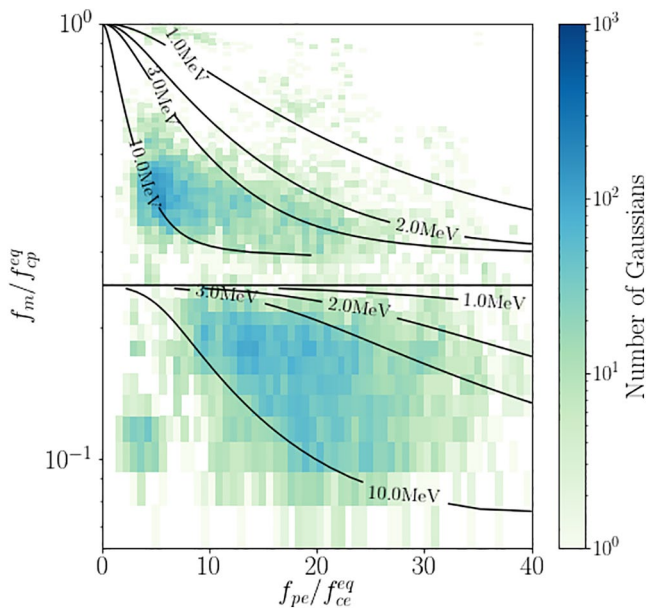


Figure 10. 2D histogram of hydrogen and helium electromagnetic ion cyclotron observations binned by f_m/f_{cp}^{eq} and f_{pe}/f_{ce}^{eq} . The corresponding electron minimum resonance energy is over-plotted in black and the helium gyrofrequency is shown by the horizontal black line.

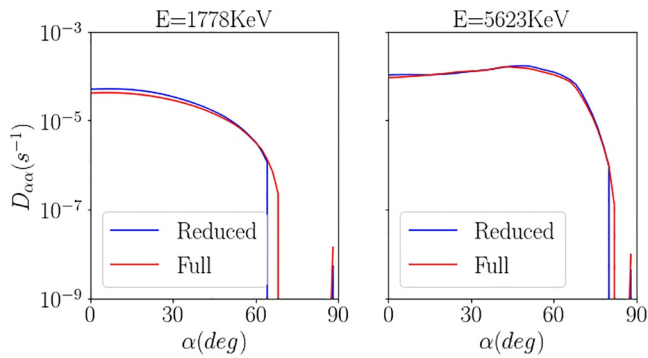


Figure 11. Comparison of full method (average of observation specific diffusion coefficients) and reduced method (wave spectra of observations summed within f_{pe}/f_{ce}^{eq} bins before calculating the diffusion coefficients in each bin and summing over bins, normalized by the number of observations) for helium band electromagnetic ion cyclotron waves at $|\lambda_m| < 5^\circ$ for $P_{dyn} > 5$ nPa and $L^* = 4.75$.

where the refractive index tends to infinity in the cold plasma approximation for oblique propagation. We discuss the sensitivity to this choice in the discussion section.

Jun et al. (2021) performed a comprehensive analysis of EMIC wave normal angles using both Van Allen Probe and Arase data. They found that the majority of hydrogen and helium band EMIC wave modes have wave normal angles of $< 30^\circ$. More oblique waves are detected near dawn at $L > 8$ (Anderson et al., 1992; Jun et al., 2021; Min et al., 2012). EMIC waves are thought to become more oblique as they propagate to higher latitudes from the equator (Anderson et al., 1992; Horne & Thorne, 1994). Gamayunov et al. (2018) noted a discrepancy between observations at low L and theory, they suggested that the superposition of multiple waves can lead to underestimation in the wavenormal angle when calculated using Fast Fourier Transforms. Ni et al. (2015) investigated the sensitivity of electron diffusion to EMIC wave normal angle and found that at $L \leq 5.5$ the decay timescales were nearly independent of the wave normal angle model at $E \geq 2$ MeV unless a very oblique wave is adopted over all latitudes. We performed calculations using the latitudinal varying wave normal angle model from Ni et al. (2015) and found minimal difference in the diffusion coefficients in the domain of interest to

the fixed wave normal angle model used by Kersten et al. (2014) and Ross et al. (2020). Therefore we assume that the waves have a Gaussian distribution in X , $X = \tan \psi$, where ψ is the wave normal angle, centered on $\psi = 0$ with a width $X_w = \tan 15^\circ$. The cut-off in X is taken to be $2X_w$. With this wave normal angle prescription, we are omitting the contribution from oblique waves near dawn in the outer magnetosphere, however, the average EMIC wave intensity is generally much lower in this region compared to the noon and the afternoon sectors (Figures 2–5).

Ross et al. (2020) demonstrated a new method of calculating diffusion coefficients for electron diffusion by EMIC waves. In these calculations, observation-specific diffusion coefficients are calculated for each observation using the observed wave spectra and plasma frequency to electron gyrofrequency ratio. The drift and bounce averaged diffusion coefficients were then calculated by averaging the bounce averaged diffusion coefficients within an L^* and activity bin. In this way, the full range of wave particle interactions resulting from the variability of the plasma environment was captured in the diffusion coefficients. However, their method is numerically expensive on large datasets as it requires the calculation of bounce averaged diffusion coefficients for each observation. Here we approximate the method from Ross et al. (2020) by binning the observations in f_{pe}/f_{ce}^{eq} and L^* allowing multiple observations to be combined into one diffusion coefficient calculation while retaining the spectral information from each observation. The EMIC observations presented in the previous section are first binned by activity (which in this study is either P_{dyn} , Kp , or Dst) and L^* (adopting the bin centered L^* value for all observations in the bin). Within each bin, we further bin the results by f_{pe}/f_{ce}^{eq} , again assigning the central bin value to f_{pe}/f_{ce}^{eq} . Given that we have point measurements, we make the assumption that the latitudinal variation of the wave is the same for each observation. As a result, the observations within a f_{pe}/f_{ce}^{eq} , activity and L^* bin only differ through their equatorial spectra. For each observation, we reconstruct the EMIC power spectral density using the Gaussian parameters and cut-offs determined from the observations (see Section 2.1). We can add the power spectral densities of each measurement in a bin and calculate the bounce averaged diffusion coefficients using this summed profile. Note that this summed profile is rarely a Gaussian but has multiple peaks, coming from individual observations. The resulting diffusion coefficients are then a close approximation of the sum of the bounce averaged diffusion coefficients calculated from the observation specific diffusion coefficients within the f_{pe}/f_{ce}^{eq} , activity and L^* bin. Finally, after summing the diffusion coefficients over the f_{pe}/f_{ce}^{eq} bins, while still retaining the L^* and activity binning, and dividing by the number of observations within the L^* and activity bin, including those with no EMIC observed activity, we have an approximation of the average observation specific diffusion coefficient. A more formal description is given Appendix A.

The error in the approximation is dependent on the granularity of the L^* and x binning, with smaller bins giving better agreement and in the limit of infinitely small bin sizes is exact. After exploring different bin sizes, we adopt L^* bins of width $0.5 L^*$ and f_{pe}/f_{ce}^{eq} bin widths of 2.5, which give very good agreement with the full calculation (Figure 11).

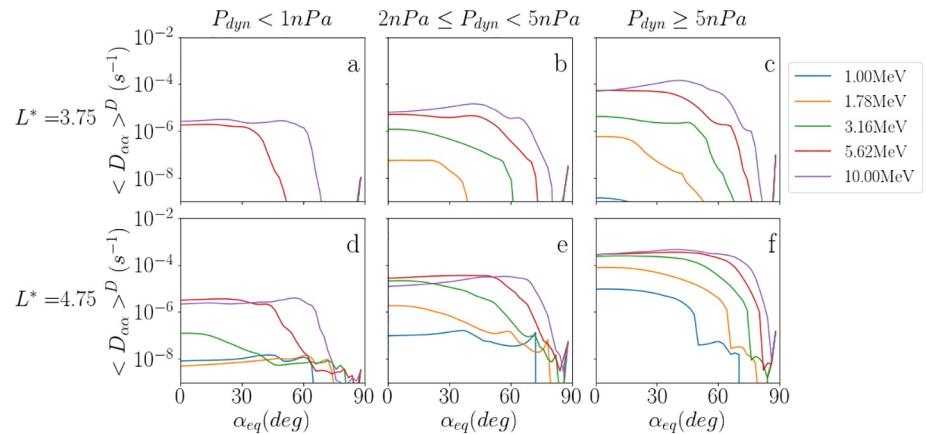


Figure 12. Bounce and drift averaged pitch-angle diffusion coefficients parameterized by P_{dyn} including both hydrogen and helium band waves.

3.2. Results

Here we present our diffusion coefficients parameterized by P_{dyn} , our results for the other parameterizations are somewhat similar and so are not shown here.

The bounce and drift averaged pitch-angle diffusion coefficients parameterized by P_{dyn} are shown in Figure 12. Electron pitch-angle diffusion by EMIC waves dominates over the energy and cross term diffusion (Glauert & Horne, 2005) and therefore we focus on pitch-angle diffusion here. Diffusion increases with increasing solar wind pressure at all energies. When $P_{dyn} < 1$ nPa at $L^* = 3.75$, there is rapid drop off in pitch-angle diffusion below 5.6 MeV, Figure 12a, even at 10 MeV diffusion is limited to $\alpha_{eq} \leq 60^\circ$ and therefore can not remove higher pitch-angled electrons. At high solar wind pressures, electrons with lower energies and higher α_{eq} are diffused. The diffusion coefficients increase with increasing L^* and extend to larger α_{eq} . For instance, at $L^* = 3.75$ when $2 \text{ nPa} \leq P_{dyn} < 5 \text{ nPa}$ (Figure 12b), diffusion of 1.78 MeV electrons (orange line) is limited to $\alpha_{eq} \leq 40^\circ$ but at $L^* = 4.75$ (Figure 12e) diffusion occurs up to near 90° , allowing for near equatorially mirroring particles to be removed from the belt.

The pitch-angle profiles of the diffusion coefficients look more irregular in profile than those calculated using average spectra which assume a single-peaked, Gaussian power distribution. This is because, in our model, there are contributions from many EMIC wave spectra, giving rise to more complex diffusion coefficient profiles.

In Section 3.1, we discussed the restricted latitude range used in this study and the rapid decrease in contribution with increasing latitude. Figure 13 shows that the diffusion coefficients decrease with latitude and the minimum resonant energy increases. The electron energies that resonate with the EMIC waves increase with increasing latitude as a result of the decreasing local wave frequency to proton gyrofrequency and plasma to electron gyrofrequency ratios, Figure 7. Additionally, the increased local pitch-angle of the particle at higher latitudes further increases the resonant energies.

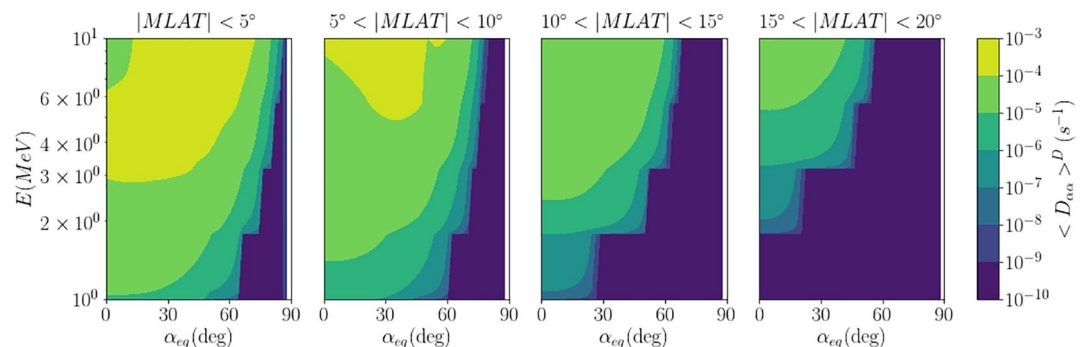


Figure 13. Contributions by magnetic latitude to the bounce and drift averaged pitch-angle diffusion coefficients parameterized by P_{dyn} for helium band waves at $L^* = 4.75$ and $P_{dyn} \geq 5$ nPa.

4. Long Term Global Radiation Belt Simulations

In this section, we explore the effect of these new diffusion coefficients on the relativistic and ultra-relativistic populations using year long global radiation belt simulations. The interval between 1 March 2015 and 1 March 2016 is chosen as it exhibits a range of dynamics including multiple active periods where there is significant acceleration up to ultra-relativistic energies followed by quiescent periods with gradual decay, allowing us to study the effects of EMIC activity during a range of magnetospheric conditions.

4.1. Method

We perform 3D simulations of the Earth's radiation belts using the British Antarctic Survey Radiation Belt Model (BAS-RBM) (Glauert et al., 2014a, 2014b) which solves the phase-averaged Fokker-Plank equation that calculates the evolution of the electron phase space density. The evolution of the phase space density, f , is given in terms of equatorial pitch-angle, α_{eq} , Roederer L^* and energy, E .

$$\begin{aligned} \frac{\partial f}{\partial t} = & \frac{1}{g(\alpha)} \frac{\partial}{\partial \alpha} \Big|_{E,L} g(\alpha) \left(D_{\alpha\alpha} \frac{\partial f}{\partial \alpha} \Big|_{E,L} + D_{\alpha E} \frac{\partial f}{\partial E} \Big|_{\alpha,L} \right) \\ & + \frac{1}{A(E)} \frac{\partial}{\partial E} \Big|_{\alpha,L} A(E) \left(D_{EE} \frac{\partial f}{\partial E} \Big|_{\alpha,L} + D_{E\alpha} \frac{\partial f}{\partial \alpha} \Big|_{E,L} \right) \\ & + L^2 \frac{\partial}{\partial L} \Big|_{\mu,J} \left(\frac{D_{LL}}{L^2} \frac{\partial f}{\partial L} \Big|_{\mu,J} \right) - \frac{f}{\tau_c} - \frac{f}{\tau_M} \end{aligned} \quad (1)$$

$$g(\alpha) = T(\alpha) \sin 2\alpha \quad (2)$$

$$A(E) = (E + E_0)(E(E + 2E_0))^{1/2} \quad (3)$$

$$T(\alpha) = (1.3802 - 0.3198(\sin \alpha + \sin^{1/2} \alpha)). \quad (4)$$

Where E_0 is the electron rest mass, τ_c and τ_M are the timescales of electron loss into the atmosphere and to the magnetopause, respectively. Here, $\mu = p^2 \sin^2 \alpha / (2m_e B_0)$ and $J = \oint p_{\parallel} ds$ are the first and second adiabatic invariants (Schulz & Lanzerotti, 1974), where m_e is the electron rest mass, B_0 is the mean value of the geomagnetic field at the Earth's surface and p 's the electron's momentum.

The fundamental equations solved by BAS-RBM are similar to other global radiation belt models such as VERB (Shprits et al., 2009), DREAM (Reeves et al., 2012), and SALAMBO (Beutier & Boscher, 1995). The models differ through their modeling of the wave-particle interactions by diffusion coefficients. Each of the global radiation belts models uses statistical models of the average wave and plasma properties to calculate the diffusion coefficients. The EMIC wave diffusion coefficients presented here are calculated in a significantly different manner where the variation in observed wave-spectra and plasma properties are included in the diffusion coefficient calculations. This is a necessary extension as the operation of calculating the diffusion coefficients and the process of averaging do not commute that is, the electron diffusion by an average wave is not equal to the average diffusion by waves (Watt et al., 2019, 2021). By taking our approach a more representative effect of electrons on the radiation belts is included.

In all of the runs below, we include hiss diffusion coefficients from Glauert et al. (2014a) which are parameterized AE*, defined as the maximum AE over the previous 3 hr, and restricted to inside the plasmopause. Chorus wave diffusion coefficients are parameterized by AE (Horne et al., 2013) and are restricted to outside the plasmopause. The plasmopause location is given by Carpenter and Anderson (1992). For radial diffusion, we use the Kp -driven magnetic component of the Brautigam and Albert (2000) formalism. The location of the last closed drift shell is calculated following the method of Glauert et al. (2014b) and effects included in the simulations.

Van Allen Probe A and B background corrected MagEIS electron flux (Claudepierre et al., 2015) and REPT electron flux (Baker et al., 2012) are used for both the initial condition and the boundary conditions at L_{\min} , L_{\max} , and E_{\min} . The inner L^* boundary is set to be inside the slot region at 2.5, and the outer L^* boundary to 5.3 which is the largest L^* consistently sampled throughout the simulation period. The minimum energy boundary is determined by assuming constant first adiabatic invariant with $E = 150$ keV at the outer L^* boundary in order to exclude lower electron energies that are influenced by physics not accounted for in the model. Note that BAS-RBM assumes a dipole magnetic field configuration internally as is usual for all global radiation belt models.

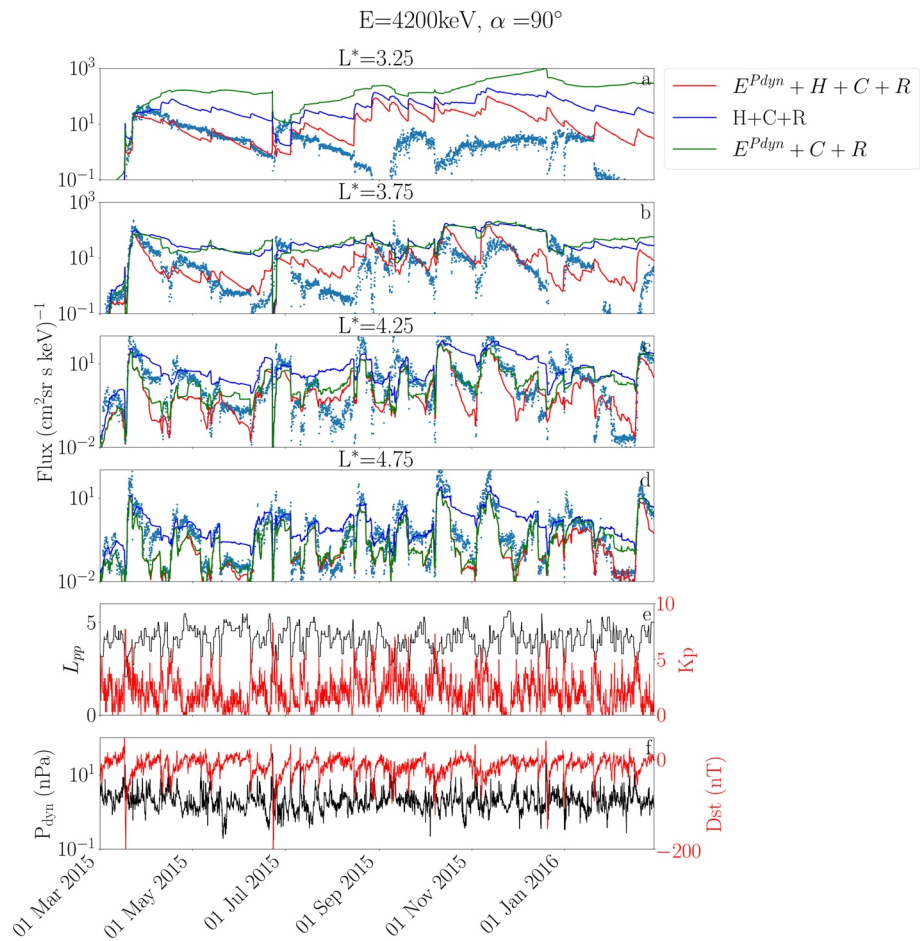


Figure 14. Panels (a)–(d) compare the modeled British Antarctic Survey Radiation Belt Model 85° 4.2 MeV electron flux against the 90° Van Allen Probe observations (blue dots) at $L^* = 3.25, 3.75, 4.25,$ and 4.75 . The Van Allen Probe observations within $0.1 L^*$ of the specified value are hourly averaged. In the legend, $E^{P_{dyn}}$ corresponds to the solar wind dynamics pressure parameterized EMIC diffusion coefficients, while H, C, and R refer to hiss waves, chorus waves, and radial diffusion respectively. Panels (e) and (f) show K_p , the plasmapause location (L_{pp}), Dst, and P_{dyn} during the period.

4.2. Contributions to Relativistic Electron Flux Decay

Both plasmaspheric hiss waves (Meredith et al., 2007; Pinto et al., 2019; Thorne et al., 2013) and EMIC waves (Drozdov et al., 2017; Kersten et al., 2014; Ma et al., 2015; Shprits et al., 2016; Usanova et al., 2014) are believed to be important for the decay of relativistic and ultrarelativistic electrons. Additionally, Wang and Shprits (2019) showed that chorus waves at high latitude can also contribute to the loss of 0.9 MeV MeV electrons. In order to assess the relative importance of these waves as a function of L^* and electron energy, we compare three simulations with the following combinations of EMIC and plasmaspheric hiss diffusion coefficients: EMIC and plasmaspheric hiss; EMIC and no plasmaspheric hiss; plasmaspheric hiss and no EMIC. Note that radial diffusion and chorus waves are included in each of these simulations. For these runs, we use our P_{dyn} parameterized EMIC wave diffusion coefficients. We focus on the near equatorially mirroring electron flux for the comparison as the decay of this flux is dependent on electron diffusion at lower pitch-angles and therefore requires an accurate model of diffusion at all pitch-angles. For BAS-RBM we take the $\alpha_{eq} = 85^\circ$ and for the Van Allen Probe observations the central pitch-angle bin.

Figure 14 shows the results for 4.2 MeV electron flux. For $L^* \geq 4.25$, losses due to EMIC and hiss waves (red curve) and EMIC waves alone (green) are much higher than losses due to hiss alone (blue). This indicates that hiss is not very effective in removing electrons at these energies. At $L^* = 3.75$ losses due to hiss and EMIC (red) remain very effective whereas losses due to hiss alone (blue) or EMIC waves alone (green) are far less effective.

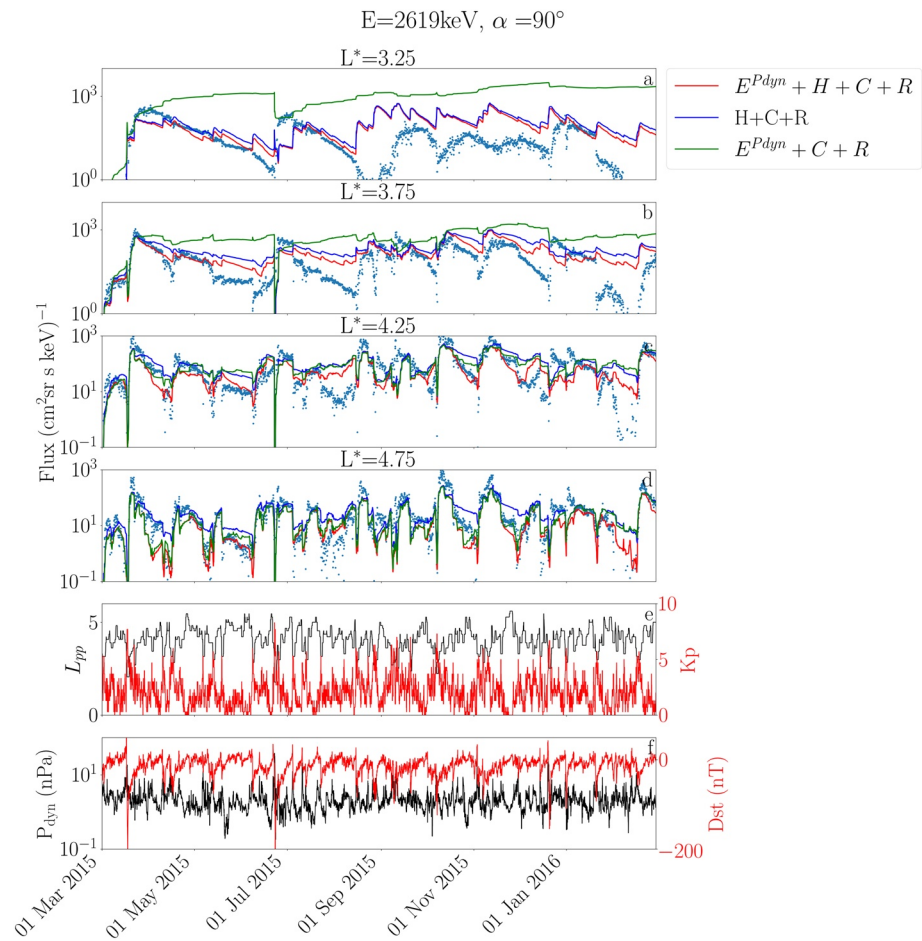


Figure 15. The same as Figure 14 but for 2.6 MeV electrons.

This indicates that the combination of the two waves modes is very important for removing electrons at large pitch angles in this region, as suggested earlier by the width of the pitch angle distribution in Figure 12. Hiss provides diffusion at pitch-angle close to 90° while EMIC waves diffuse the particles at lower pitch-angles. At $L^* = 3.25$ initially, the best agreement between the data and the model is for hiss and EMIC (red) which give the largest losses for the whole period compared to those wave modes on their own. Between 1 March and the middle of August the combined hiss and EMIC model does better than the other two models, but after that, all three models show several rapid increases in flux whereas there is a large reduction and drop out in the data in early September followed by a more gradual increase that is not reproduced. It is interesting to note that the data show a significant increase in flux at $L^* = 3.75$ compared to a reduction at 3.25. Since EMIC and hiss waves contribute mainly to electron loss and not acceleration, the increase in flux in the model is due to inward radial diffusion as shown in the discussion. This suggests that the radial diffusion coefficients used in this model, and in many other global models, needs to be substantially improved for low L^* . Note that the divergence of the model from the observation does not correspond to the largest Kp when D_{LL} is at its largest. We return to this in the discussion.

Figure 15 shows the results for 2.6 MeV. At $L^* = 4.75$ the model results for EMIC and hiss (red) and EMIC alone (green) are very similar and reproduce the flux variations quite well indicating that EMIC waves are the most important in this region. In contrast, hiss alone (blue) is able to reproduce some but not all of the decay. A similar result is obtained at $L^* = 4.25$. However at lower $L^* \leq 3.75$ the EMIC and hiss model performs the best and the model for EMIC waves alone (green) does not capture the decay. The results illustrate that EMIC waves acting alone are not very effective at causing loss at energies of a few MeV, rather the combined action of hiss waves and EMIC waves is necessary to explain the observed decay.

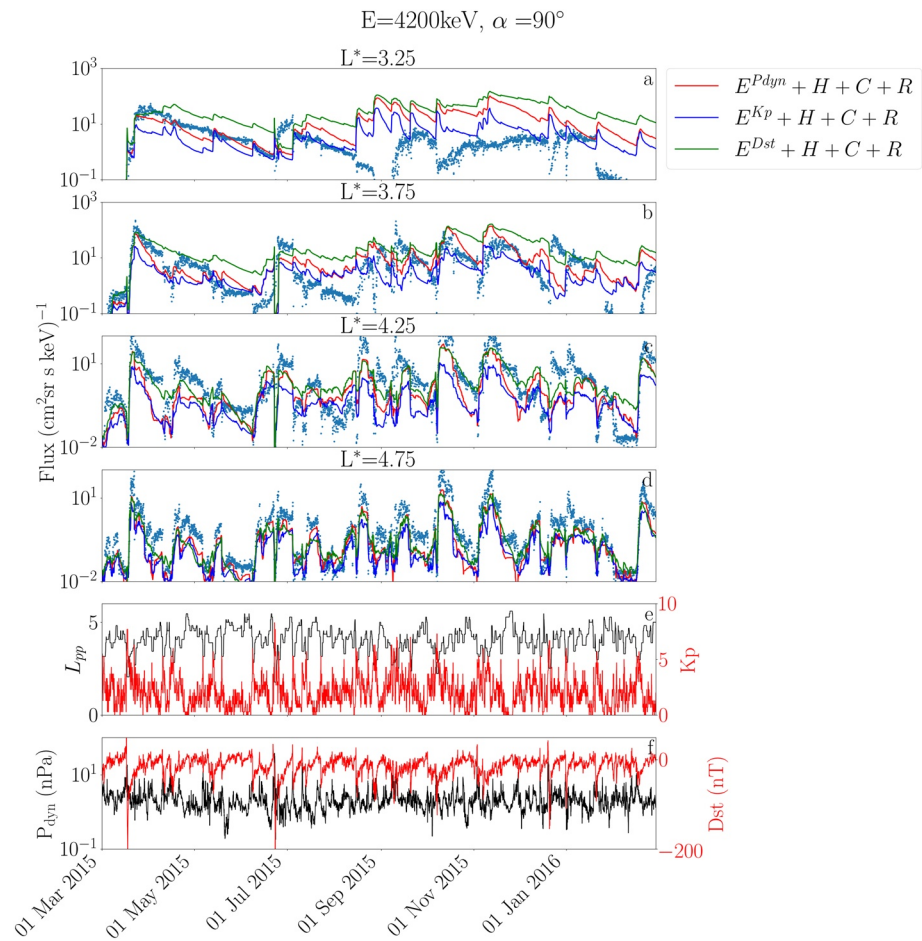


Figure 16. The 85° 4.2 MeV electron flux was calculated by the British Antarctic Survey Radiation Belt Model at $L^* = 3.25$, 3.75, 4.25, and 4.75 compared against the 90° Van Allen Probe observations (blue). The red, blue, and green lines are from the simulations with electromagnetic ion cyclotron waves parameterized by P_{dyn} , Kp , and Dst , respectively.

4.2.1. Activity Parameterization

As described in Section 3, we have calculated 3 separate EMIC diffusion coefficients, parameterized by P_{dyn} (as used in the previous section), Kp and Dst . Here we compare these parameterizations and their agreement with Van Allen Probe observations to determine which parameterizations work the best. In the previous section, we found that the impact of EMIC waves is easily identifiable at 4.2 MeV and $L^* \geq 3.25$, in which case we focus our analysis of the EMIC driving parameter on this energy channel.

Figure 16 shows the 4.2 MeV electron flux with EMIC waves parameterized by P_{dyn} (red), Kp (blue), and Dst (green). At $L^* \geq 4.25$, all three simulations perform well and there is little difference between the parameterizations, although the simulation Kp driven EMIC waves typically under estimates the peak electron flux by a greater amount than the other simulations. At lower $L^* \leq 3.75$ (Figures 16a and 16b) the Kp and P_{dyn} parameterizations perform significantly better than the Dst parameterization, with the Dst parameterization systematically overestimating the flux. The P_{dyn} and Kp driven models at $L^* = 3.75$ agree fairly well with the observations. Again, at $L^* = 3.25$, there is good agreement between the P_{dyn} and Kp model runs compared to the observations until August 2015, with decay rates consistent with those observed.

4.3. Metrics

In order to assess the EMIC models, we make use of the metrics from Morley et al. (2018) and Glauert et al. (2018), namely, the median symmetric accuracy (MSA) and the symmetric signed bias (SSPB). Both of these metrics are

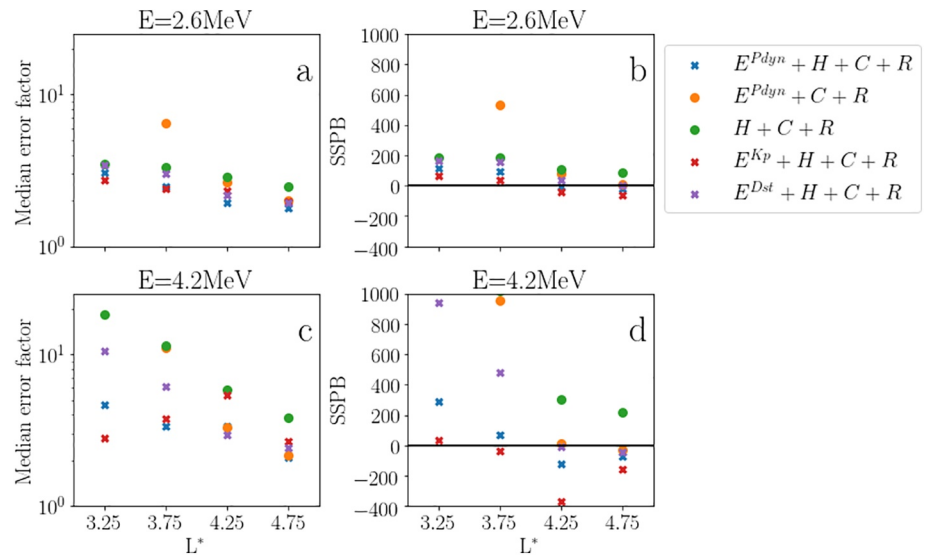


Figure 17. Median error factors and signed symmetric percentage bias for the British Antarctic Survey Radiation Belt Model runs compared to Van Allen Probe data. Note that the P_{dyn} no hiss simulation at $L^* \leq 3.75$ is off the scale in the positive direction in each plot and is omitted for clarity.

straight-forward to interpret, symmetric when penalizing under and over prediction, and robust to outliers. The median symmetric accuracy is given by

$$MSA = 100[\exp(\text{Median}\{|\ln Q_i|\}) - 1] \quad (5)$$

with $Q_i = X_i/Y_i$ with Y_i denoting the model value and X_i the observation. It is informative to note that 50% of results are with a factor $\exp(\text{Median}\{|\ln Q_i|\}) = 1 + \text{MSA}/100$ of the data, referred to as the median error factor. The SSPB gives the percentage overestimate or underestimate by the given percentage of the median error and is defined as

$$\text{SSPB} = 100\text{sgn}(\text{Median}\{|\ln Q_i|\})\exp(\text{Median}\{|\ln Q_i|\}) - 1. \quad (6)$$

The metrics are applied to near equatorially mirroring electron flux, namely, the differential $\alpha_{eq} = 85^\circ$ electron flux modeled by BAS-RBM is compared to the 90° flux measurement observed by the Van Allen Probes.

Figures 17a and 17b show that the median error factors and SSPBs for 2.6 MeV electrons at $L^* \leq 3.75$ are small when hiss waves are included (blue crosses) compared to when they are omitted (orange dots). In contrast, including EMIC waves has little effect on the metrics (blue crosses compared to green dots). At larger L^* , both EMIC waves and hiss waves are important with the smallest errors when both waves are included (blue crosses compared to orange and green dots). For 4.2 MeV electrons, Figures 17c and 17d, including EMIC waves significantly improve the metrics at $L^* \leq 3.75$ (blue crosses compared to green dots), although hiss waves are also very important for reducing the errors and biases (blue crosses compared to orange dots). At $L^* \geq 4.25$, omitting hiss waves (orange dots) has minimal effect on the metrics and achieves similar scores to an identical simulation where they are included (blue crosses), while if EMIC waves are left out (green dots) the errors and bias are much greater. The importance of both EMIC waves and hiss waves for the decay of multi-MeV electron fluxes is consistent with the conclusions of Drozdov et al. (2020) based on long-term simulations, with the EMIC waves providing rapid losses close to the loss cone and hiss waves contributing to electron diffusion at larger pitch-angles.

At $L^* \geq 4.25$, the simulations with EMIC waves parameterized with P_{dyn} (blue crosses), Kp (red crosses), and Dst (purple crosses) perform comparably well, although Kp has a significant negative SSPB for 4.2 MeV electrons at $L^* = 4.25$ which is related to the lower flux shown by the blue line in Figure 16d. At $L^* \leq 3.75$, the P_{dyn} and Kp simulations perform better than the Dst simulation with substantially lower median error factors and SSPBs.

5. Discussion

Figure 9 clearly shows EMIC waves are organized by plasma density, with hydrogen band waves in low density regions such as the plasma trough while helium band waves are in high-density regions such as the plasmasphere and plasma plumes (Anderson et al., 1992; Zhang et al., 2016). However, we do not parameterize the waves by density, instead, we parameterize by solar or geomagnetic activity, and the spread in plasma environment is captured in the model, due to the way we calculate our drift-averaged DC from observations specific diffusion coefficients which sample from all MLTs, which is not captured in previous average statistical models.

Results from numerical diffusion experiments (Watt et al., 2021) indicate that averaging observation-specific diffusion coefficients may be appropriate if the wave activity varies sufficiently rapidly, even given a large amount of variability in observations of wave intensity and plasma conditions and no further parameterization. The parameterizations investigated here remove some sources of variability and can be used to construct more accurate models. Further investigations into the temporal and spatial variability of diffusion coefficients for EMIC waves using the observations shown here and results from for example, Blum et al. (2017) would also confirm whether the averaging strategy used here is most accurate. There is no denying that the creation of a deterministic model of averaged diffusion coefficients is much more tractable and appealing than using multiple stochastic parameterizations (Watt et al., 2021) to capture all variability in the wave-particle interactions important to Earth's radiation belts.

EMIC waves that approach their upper bounding gyrofrequency are affected by warm plasma. Cold plasma theory, as used in this study, breaks down in this limit as the refractive index tends to infinity when the wave frequency approaches the gyrofrequency. To avoid invalidating the approximation, we have set the upper cut-off to be $f_{up} = 0.97f_{ci}$. However, the exact threshold at which cold plasma theory breaks down depends on the plasma properties. We, therefore, test the sensitivity of our results to the imposed threshold and perform an identical set of diffusion coefficient calculations parameterized by P_{dyn} with $f_{up} = 0.95f_{ci}$. There is a negligible difference between the two model results (not shown) giving us confidence that results robust to this assumption.

Shprits et al. (2013) considered the energy range of electrons that interact with whistler mode waves compared to EMIC waves during a long lasting third radiation belt in September 2012. They concluded that at $L \sim 3.3$ whistler mode waves were able to resonate with electrons at relativistic energies (<2 MeV) and but were unable to do so with ultrarelativistic electrons (>2 MeV) near the equator. Instead, they suggested that EMIC waves are important for the decay of the third belt at ultrarelativistic energies (Shprits et al., 2016, 2018). Our results here are consistent with Shprits et al. (2013) at $L \sim 3.3$, but also show that the electron energy range that are significantly affected by EMIC waves depends on L^* as a result of the increasing f_{pe}/f_{ce} with L^* , allowing for substantial electron diffusion at $\lesssim 2$ MeV and $L^* \geq 4.0$.

The global radiation belt simulations with EMIC waves parameterized by Kp underestimate peak electron flux more than when Dst and P_{dyn} are used. This may be due to overestimating EMIC losses outside of the plasmasphere, removing the electrons that are being accelerated by chorus waves and radial diffusion. Kp is typically enhanced for longer than P_{dyn} while Dst recovers more quickly. Therefore EMIC waves in the Kp driven simulation are able to counteract electron acceleration by chorus waves and radial diffusion for longer, suppressing the build-up of relativistic electrons. Alternatively, as the chorus diffusion model does not include variability in plasma density, other than through variation in the MLT, acceleration up to MeV energies may be under represented (Allison et al., 2021).

At $L^* \leq 3.75$, the Dst simulation performs significantly worse than the other 2 simulations, while the Kp simulation performs the best (Figure 17). The greater overestimation of the flux in the Dst simulation is likely partly due to the larger reservoir of flux at higher L^* , compared to the Kp and P_{dyn} simulations, that is diffused inward. In Figure 6 we showed that Dst is a weaker indicator of EMIC wave activity, and hence electron diffusion, than both Kp and P_{dyn} , particularly at $L^* \geq 4.25$. The weaker dependence of EMIC wave activity on Dst may be related to the inability of the Dst index to capture high-speed-stream-driven geomagnetic storms (Borovsky & Denton, 2010; Borovsky & Shprits, 2017) which can drive enhanced EMIC activity (Gamayunov et al., 2020) and are associated with a daylong increase in solar wind pressure at storm onset. Furthermore, Borovsky (2017) found that the correlation between radiation belt flux and Kp is much stronger than the correlation with Dst suggesting that the Dst index is insufficient to characterize the radiation belts.

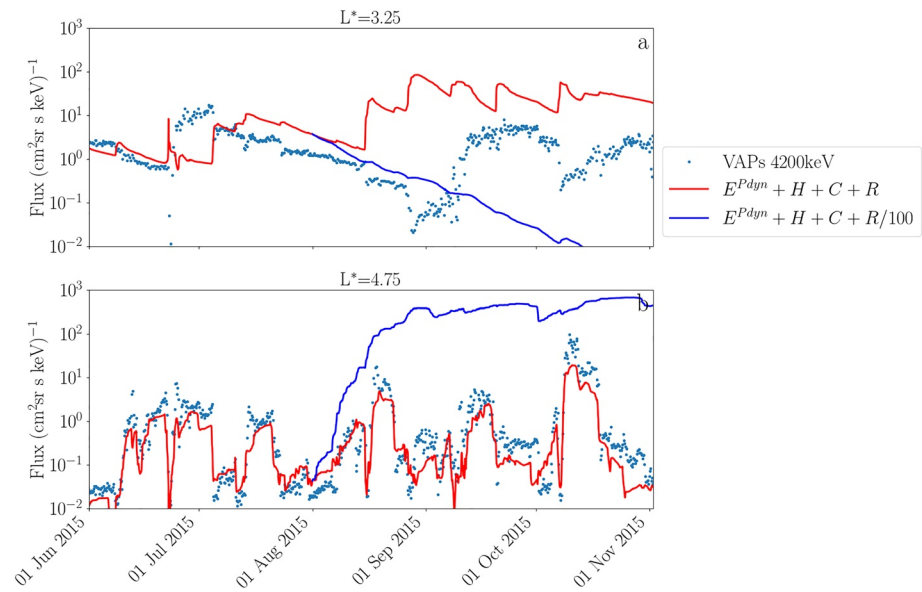


Figure 18. The 85° 4.2 MeV electron flux was calculated by British Antarctic Survey Radiation Belt Model at $L^* = 3.25$ and 4.75 compared against the 90° Van Allen Probe observations (blue). The red lines show the results from the simulation with electromagnetic ion cyclotron, hiss and chorus wave, and radial diffusion. The blue lines are from a simulation with radial diffusion reduced by a factor of 100 from 1 August 2015.

We obtain good agreement with observations in our long-term simulations with EMIC waves parameterized by P_{dyn} . Drozdov et al. (2017) performed long-term Fokker-Planck simulations of the radiation belts using the VERB code comparing EMIC waves parameterized by Kp , Dst, and AE indices, solar wind velocity, and solar wind pressure. In their study, they used a representative EMIC spectral profile and an average plasma density for their EMIC diffusion coefficient calculations. They minimized the absolute mean error by optimizing the wave amplitude and activity threshold for the presence of EMIC waves. They found that solar wind dynamic pressure provides the best parameterization of EMIC waves. Our Van Allen Probe EMIC data set shows significantly increased EMIC activity during magnetospheric compression (Figure 4), consistent with previous statistical results (Anderson & Hamilton, 1993; J. V. Olson & Lee, 1983; Saikin et al., 2016; Usanova et al., 2012). Furthermore, the average wave intensity increases with solar wind pressure, even at $L^* < 4$, which in turn leads to faster rates of electron diffusion. EMIC waves at low L^* s have previously been linked with magnetospheric compressions; Qin et al. (2019) found EMIC waves at $1.9 < L^* < 3.2$ during extreme magnetospheric compression on 22 June 2015. However, it is unlikely that solar wind pressure can generally directly lead to EMIC waves at $L^* < 4.0$ as moderate magnetospheric compression will only affect the outer magnetosphere. Rather, it is likely that solar wind pressure is correlated with geomagnetic conditions which are favorable for EMIC wave activity at lower L^*

In Figures 14–16 we showed that the modeled >2.6 MeV electron flux at $L^* \geq 3.75$ agree well with the Van Allen Probe observations. However, at $L^* = 3.25$ (e.g., Figure 16a) we obtain sudden increases in >2.6 MeV electron flux during August 2015 that are not observed in the Van Allen Probe data. Instead, the observations show a gradual increase in flux on a day to week timescale. Contrastingly, observations of lower energy flux (<1 MeV) do show a sudden increase in flux (not shown) which agrees well with the modeled flux. This suggests that we are missing or poorly capturing the physical processes governing the MeV population during this period. In Figure 18a we show results (blue line) from a simulation with radial diffusion reduced by a factor of 100 from the 1 August 2015. The flux no longer shows the sudden increases found previously (red line) implying these increases are a result of transport by radial diffusion. Similarly, later in the simulation with radial diffusion, there are additional increases in the modeled flux $L^* = 3.25$ which are also not observed. Two possibilities explain these differences. The radial diffusion model may break down at several MeV energies in this region (Lejosne et al., 2013) or losses by local wave-particle interactions during this period are sufficiently strong and localized to $L^* \sim 3.25$ to counter act the flux increase by radial diffusion. The ratio of f_{pe}/f_{ce} is generally low at $L^* \sim 3.25$ and exceeds 12 only 20% of the time at (Figure 9c) and, therefore, unless there is substantial wave power very close to the gyrofrequency, the 2.6 MeV electrons will not be diffused by EMIC waves at these low densities

(Figure 10). Furthermore, there is no evidence for strong EMIC waves close to an upper bounding gyrofrequency during these times. If the differences were due to hiss waves then the increase in flux at lower energies would also be reduced. It is therefore more likely the discrepancy is a result of radial diffusion rather than diffusion by local wave-particle interactions.

The pitch-angle and energy of the electrons that can resonate with an EMIC wave depend on the cold ion composition. Measurements of the cold ion composition are particularly difficult due to satellite charging (Olsen et al., 1985) preventing reliable direct measurements. Warm ion measurements can be made but they may differ significantly from the cold ion population that dominates the mass. Therefore, we are unable to use the ion composition observed during each observation to complement the observation-specific wave spectra and plasma density. In this study we have adopted the ion composition from Kersten et al. (2014) however a range of fixed values have previously been adopted (Ma et al., 2015; Meredith et al., 2003; Summers & Thorne, 2003). A higher He + percentage leads to electron diffusion at lower energies for helium EMIC waves but the converse for hydrogen EMIC waves.

By the very nature of a statistical model, we are averaging over many events within an activity and L^* bin. In a statistical approach parameterized by a geomagnetic activity index or solar wind measurement, we are assuming that the index captures the variation and captures the average response of the electron population under those conditions. The true state of the system however may not always be well represented by a statistical model. For the case of EMIC waves, the growth of the EMIC waves depends on the ion temperature anisotropy and electron plasma density. Similarly, the wave-particle interactions depend on electron plasma density and ion composition. In turn, the ion population and electron plasma density are affected by the time history of the magnetosphere through electric fields and disturbances in the magnetic field. Under different magnetospheric driving, these populations will evolve differently leading to different EMIC wave behavior (Gamayunov et al., 2020) which will not necessarily be well captured in a statistical model of this form. Coupled ring current—plasmaspheric models (Jordanova et al., 2008) provide a means to include these effects more consistently however it is challenging to constrain such models due to the number of degrees of freedom.

6. Conclusions

We have analyzed the L^* dependence of the wave spectra and the corresponding plasma frequency to electron gyrofrequency ratio of EMIC waves observed by the Van Allen Probe A satellite. These observations have then been used to calculate bounce and drift averaged EMIC diffusion coefficients from averaging observation specific diffusion coefficients. When calculated in this way, the variability in wave spectra and plasma density is included in the diffusion coefficients. These have been included in a global radiation belt model, BAS-RBM, and year long simulations compared against Van Allen Probe observations to determine at what energies and L^* s EMIC waves are important and which activity parametrization gives the best agreement. Our principle results are as follows:

1. For $L^* > 4$ the average plasma frequency to electron gyrofrequency ratio for helium band EMIC waves is much higher than statistical plasmaspheric models, while hydrogen band waves are typically in low density regions.
2. EMIC waves do not contribute significantly to the decay of the ultrarelativistic storage ring at 2.6 MeV due to the low values of f_{pe}/f_{ce} in the region, instead diffusion by hiss waves is the dominant loss process. In comparison, EMIC wave and hiss waves are both necessary for the decay of the 4.2 MeV component of the storage ring.
3. At $L^* \geq 4.25$, electron flux decay is largely controlled by EMIC waves at ≥ 4.2 MeV, but a combination of hiss waves and EMIC waves determine the electron losses at 2.6 MeV.

Appendix A: Reduced Diffusion Coefficient Method

For observation i , let the bounce averaged diffusion coefficients be denoted by

$$D_i = D(L_i^*, x_i, (B_{w,i}^{eq})^2) \quad (\text{A1})$$

where we have dropped the α , E assumed dependence and we have defined $x_i = f_{pe,i}/f_{ce,i}^{eq}$ for brevity. D is the bounce average diffusion operator assuming that ion composition is constant between observations and that the latitudinal variation of the wave normal angle is the same between observations.

Now consider a specific activity bin and L^* bin, and label the set of point in this bin as \mathcal{A} and \mathcal{L} , respectively. The average of the observation specific diffusion coefficients within that bin is then given by

$$D(\mathcal{A}, L^*) = \sum_{i \in \mathcal{A} \cap \mathcal{L}} D_i / \sum_{i \in \mathcal{A} \cap \mathcal{L}} 1 \quad (\text{A2})$$

where the summation includes all observations, even those without observed EMIC waves. Note that calculating the numerator involves calculating bounce averaged diffusion coefficients for each observation. For large datasets, this becomes computationally heavy and therefore we make a series of approximations to reduce the number of calculations that are necessary.

First, we adopt the central L^* bin value, \bar{L}^* , for observations in a L^* bin. The bounce average diffusion coefficient then only depends on x_i and $(B_{w,i}^{eq})^2$. Furthermore, if the observations are now binned by x , into bins labeled \mathcal{X}_k , and the bin center values, \bar{x}_k , are adopted for all x_i in each \mathcal{X}_k , then the bounce averaged diffusion coefficients within that density bin only depend on $(B_{w,i}^{eq})^2$. We can now use the fact that operator D is directly proportional to $(B_{w,i}^{eq})^2$ to rewrite the numerator of Equation A2 as

$$\begin{aligned} \sum_{i \in \mathcal{A} \cap \mathcal{L}} D_i &= \sum_{i \in \mathcal{A} \cap \mathcal{L}} D(L^*, x_i, (B_{w,i}^{eq})^2) \\ &\approx \sum_{\mathcal{X}_k} \sum_{i \in \mathcal{A} \cap \mathcal{L} \cap \mathcal{X}_k} D(\bar{L}^*, \bar{x}_k, (B_{w,i}^{eq})^2) \\ &= \sum_{\mathcal{X}_k} D\left(\bar{L}^*, \bar{x}_k, \sum_{i \in \mathcal{A} \cap \mathcal{L} \cap \mathcal{X}_k} (B_{w,i}^{eq})^2\right). \end{aligned} \quad (\text{A3})$$

Data Availability Statement

The diffusion coefficients shown in this paper can be downloaded from the UK Polar Data Centre (<https://doi.org/10.5285/cc48c65d-5395-45a1-a60a-3a4b987fd673>).

Acknowledgments

The authors acknowledge OMNIWeb (<https://omniweb.gsfc.nasa.gov>) for the geomagnetic and solar wind indices used in this study. The research leading to these results has received funding from the National Environment Research Council Highlight Topic grant NE/P10738X/1 (Rad-Sat), National Environment Research Council grant NE/R016445/1 and NE/R016038/1. The authors are grateful for the use of Van Allen Probes data the Level 3 and Level 4 EMFISIS magnetometer data obtained from <http://emfisis.physics.uiowa.edu/data/index>.

References

- Allison, H. J., Shprits, Y. Y., Zhelavskaya, I. S., Wang, D., & Smirnov, A. G. (2021). Gyroresonant wave-particle interactions with chorus waves during extreme depletions of plasma density in the van allen radiation belts. *Science Advances*, *17*, eabc0380.
- Anderson, B. J., Erlanson, R. E., & Zanetti, L. J. (1992). 3A statistical study of pc 1-2 magnetic pulsations in the equatorial magnetosphere: 1. equatorial occurrence distributions. *Journal of Geophysical Research: Space Physics*, *97*, 3075–3088. <https://doi.org/10.1029/91ja02706>
- Anderson, B. J., & Hamilton, D. C. (1993). Electromagnetic ion cyclotron waves stimulated by modest magnetospheric compressions. *Journal of Geophysical Research*, *98*, 11369. <https://doi.org/10.1029/93ja00605>
- Baker, D. N., Erickson, P. J., Fennell, J. F., Foster, J. C., Jaynes, A. N., & Verronen, P. T. (2018). Space weather effects in the Earth's radiation belts. *Space Science Reviews*, *214*, 17. <https://doi.org/10.1007/s11214-017-0452-7>
- Baker, D. N., Kanekal, S. G., Hoxie, V. C., Batiste, S., Bolton, M., Li, X., et al. (2012). The Relativistic Electron-Proton Telescope (REPT) Instrument on Board the Radiation Belt Storm Probes (RBSP) spacecraft: Characterization of Earth's radiation belt high-energy particle populations. In Fox N. & Burch J.L. (eds.), *The Van Allen Probes Mission*. Springer, Boston. https://doi.org/10.1007/978-1-4899-7433-4_11
- Beutier, T., & Boscher, D. (1995). A three-dimensional analysis of the electron radiation belt by the salammbô code. *Journal of Geophysical Research*, *100*, 14853. <https://doi.org/10.1029/94ja03066>
- Blum, L. W., Bonnell, J. W., Agapitov, O., Paulson, K., & Kletzing, C. (2017). 2Emic wave scale size in the inner magnetosphere: Observations from the dual Van Allen Probes. *Geophysical Research Letters*, *44*, 1227–1233. <https://doi.org/10.1002/2016GL072316>
- Borovsky, J. E. (2017). Time-integral correlations of multiple variables with the relativistic-electron flux at geosynchronous orbit: The strong roles of substorm-injected electrons and the ion plasma sheet. *Journal of Geophysical Research: Space Physics*, *122*, 11961–12011. <https://doi.org/10.1002/2017JA024476>
- Borovsky, J. E., & Denton, M. H. (2010). Magnetic field at geosynchronous orbit during high-speed stream-driven storms: Connections to the solar wind, the plasma sheet, and the outer electron radiation belt. *Journal of Geophysical Research: Space Physics*, *115*. <https://doi.org/10.1029/2009JA015116>
- Borovsky, J. E., & Shprits, Y. Y. (2017). Is the Dst index sufficient to define all geospace storms? *Journal of Geophysical Research: Space Physics*, *122*, 11543–11547. <https://doi.org/10.1002/2017JA024679>
- Bortnik, J., Cutler, J. W., Dunson, C., & Bleier, T. E. (2007). An automatic wave detection algorithm applied to pc1 pulsations. *Journal of Geophysical Research: Space Physics*, *4112*. <https://doi.org/10.1029/2006JA011900>

- Brautigam, D. H., & Albert, J. M. (2000). Radial diffusion analysis of outer radiation belt electrons during the October 9, 1990, magnetic storm. *Journal of Geophysical Research: Space Physics*, *105*, 291–309. <https://doi.org/10.1029/1999ja900344>
- Carpenter, D. L., & Anderson, R. R. (1992). An ISEE/whistler model of equatorial electron density in the magnetosphere. *Journal of Geophysical Research*, *97*, 1097. <https://doi.org/10.1029/91ja01548>
- Chen, H., Gao, X., Lu, Q., & Wang, S. (2019). Analyzing ionic waves in the inner magnetosphere using long-term Van Allen Probes observations. *Journal of Geophysical Research: Space Physics*, *9124*, 7402–7412. <https://doi.org/10.1029/2019JA026965>
- Claudepierre, S. G., O'Brien, T. P., Blake, J. B., Fennell, J. F., Roeder, J. L., Clemmons, J. H., et al. (2015). A background correction algorithm for Van Allen Probes magnetis electron flux measurements. *Journal of Geophysical Research: Space Physics*, *120*, 5703–5727. <https://doi.org/10.1002/2015JA021171>
- Drozhdov, A. Y., Shprits, Y. Y., Usanova, M. E., Aseev, N. A., Kellerman, A. C., & Zhu, H. (2017). Emission wave parameterization in the long-term verb code simulation. *Journal of Geophysical Research: Space Physics*, *8122*, 8488–8501. <https://doi.org/10.1002/2017JA024389>
- Drozhdov, A. Y., Usanova, M. E., Hudson, M. K., Allison, H. J., & Shprits, Y. Y. (2020). The role of hiss, chorus, and ionic waves in the modeling of the dynamics of the multi-MeV radiation belt electrons. *Journal of Geophysical Research: Space Physics*, *9125*. <https://doi.org/10.1029/2020JA028282>
- Gamayunov, K. V., Engebretson, M. J., & Elkington, S. R. (2020). Emission waves in the earth's inner magnetosphere as a function of solar wind structures during solar maximum. *Journal of Geophysical Research: Space Physics*, *9125*. <https://doi.org/10.1029/2020JA027990>
- Gamayunov, K. V., Min, K., Saikin, A. A., & Rassoul, H. (2018). Generation of EMIC waves observed by Van Allen Probes at low L shells. *Journal of Geophysical Research: Space Physics*, *123*, 8533–8556. <https://doi.org/10.1029/2018JA025629>
- Glauert, S. A., & Horne, R. B. (2005). Calculation of pitch angle and energy diffusion coefficients with the padie code. *Journal of Geophysical Research: Space Physics*, *110*. <https://doi.org/10.1029/2004JA010851>
- Glauert, S. A., Horne, R. B., & Meredith, N. P. (2014a). Simulating the earth's radiation belts: Internal acceleration and continuous losses to the magnetopause. *Journal of Geophysical Research: Space Physics*, *119*, 7444–7463. <https://doi.org/10.1002/2014JA020092>
- Glauert, S. A., Horne, R. B., & Meredith, N. P. (2014b). Three-dimensional electron radiation belt simulations using the bas radiation belt model with new diffusion models for chorus, plasmaspheric hiss, and lightning-generated whistlers. *Journal of Geophysical Research: Space Physics*, *119*, 268–289. <https://doi.org/10.1002/2013JA019281>
- Glauert, S. A., Horne, R. B., & Meredith, N. P. (2018). A 30-year simulation of the outer electron radiation belt. *Space Weather*, *16*, 1498–1522. <https://doi.org/10.1029/2018SW001981>
- Halford, A. J., Fraser, B. J., & Morley, S. K. (2010). Emission wave activity during geomagnetic storm and nonstorm periods: Crres results. *Journal of Geophysical Research: Space Physics*, *115*, a–n. <https://doi.org/10.1029/2010JA015716>
- Horne, R. B., Kersten, T., Glauert, S. A., Meredith, N. P., Boscher, D., Sicard-Piet, A., et al. (2013). A new diffusion matrix for whistler mode chorus waves. *Journal of Geophysical Research: Space Physics*, *118*, 6302–6318. <https://doi.org/10.1002/jgra.50594>
- Horne, R. B., & Thorne, R. M. (1994). Convection instabilities of electromagnetic ion cyclotron waves in the outer magnetosphere. *Journal of Geophysical Research: Space Physics*, *99*, 17259–17273. <https://doi.org/10.1029/94ja01259>
- Horne, R. B., Thorne, R. M., Glauert, S. A., Albert, J. M., Meredith, N. P., & Anderson, R. R. (2005). Timescale for radiation belt electron acceleration by whistler mode chorus waves. *Journal of Geophysical Research: Space Physics*, *110*. <https://doi.org/10.1029/2004JA010811>
- Horne, R. B., Thorne, R. M., Shprits, Y. Y., Meredith, N. P., Glauert, S. A., Smith, A. J., et al. (2005). Wave acceleration of electrons in the Van Allen radiation belts. *Nature*, *437*, 227–230. <https://doi.org/10.1038/nature03939>
- Jordanova, V. K., Albert, J., & Miyoshi, Y. (2008). Relativistic electron precipitation by ionic waves from self-consistent global simulations. *Journal of Geophysical Research: Space Physics*, *113*. <https://doi.org/10.1029/2008JA013239>
- Jun, C. W., Miyoshi, Y., Kurita, S., Yue, C., Bortnik, J., Lyons, L., et al. (2021). The characteristics of ionic waves in the magnetosphere based on the van allen probes and arase observations. *Journal of Geophysical Research: Space Physics*, *6126*. <https://doi.org/10.1029/2020JA029001>
- Jun, C. W., Yue, C., Bortnik, J., Lyons, L. R., Nishimura, Y., Kletzing, C., et al. (2019). A statistical study of ionic waves associated with and without energetic particle injection from the magnetotail. *Journal of Geophysical Research: Space Physics*, *124*, 433–450. <https://doi.org/10.1029/2018JA025886>
- Kersten, T., Horne, R. B., Glauert, S. A., Meredith, N. P., Fraser, B. J., & Grew, R. S. (2014). Electron losses from the radiation belts caused by ionic waves. *Journal of Geophysical Research: Space Physics*, *119*, 8820–8837. <https://doi.org/10.1002/2014JA020366>
- Kletzing, C. A., Kurth, W. S., Acuna, M., MacDowall, R. J., Torbert, R. B., Averkamp, T., et al. (2013). The electric and magnetic field instrument suite and integrated science (EMFISIS) on RBSP. *Space Science Reviews*, *179*, 127–181. <https://doi.org/10.1007/s11214-013-9993-6>
- Kurth, W. S., Pascuale, S. D., Faden, J. B., Kletzing, C. A., Hospodarsky, G. B., Thaller, S., & Wygant, J. R. (2015). Electron densities inferred from plasma wave spectra obtained by the waves instrument on Van Allen probes. *Journal of Geophysical Research: Space Physics*, *120*, 904–914. <https://doi.org/10.1002/2014JA020857>
- Lejosne, S., Boscher, D., Maget, V., & Rolland, G. (2013). Deriving electromagnetic radial diffusion coefficients of radiation belt equatorial particles for different levels of magnetic activity based on magnetic field measurements at geostationary orbit. *Journal of Geophysical Research: Space Physics*, *118*, 3147–3156. <https://doi.org/10.1002/jgra.50361>
- Lyons, L. R., & Thorne, R. M. (1972). Parasitic pitch angle diffusion of radiation belt particles by ion cyclotron waves. *Journal of Geophysical Research*, *77*, 5608–5616. <https://doi.org/10.1029/ja077i028p05608>
- Ma, Q., Li, W., Thorne, R. M., Ni, B., Kletzing, C. A., Kurth, W. S., et al. (2015). Modeling inward diffusion and slow decay of energetic electrons in the earth's outer radiation belt. *Geophysical Research Letters*, *42*, 987–995. <https://doi.org/10.1002/2014GL062977>
- Mauk, B. H., Fox, N. J., Kanekal, S. G., Kessel, R. L., Sibeck, D. G., & Ukhorskiy, A. (2013). Science objectives and rationale for the radiation belt storm probes mission. *Space Science Reviews*, *179*, 3–27. <https://doi.org/10.1007/s11214-012-9908-y>
- Means, J. D. (1972). Use of the three-dimensional covariance matrix in analyzing the polarization properties of plane waves. *Journal of Geophysical Research*, *77*, 5551–5559. <https://doi.org/10.1029/ja077i028p05551>
- Meredith, N. P., Horne, R. B., Glauert, S. A., & Anderson, R. R. (2007). Slot region electron loss timescales due to plasmaspheric hiss and lightning-generated whistlers. *Journal of Geophysical Research: Space Physics*, *8112*. <https://doi.org/10.1029/2007JA012413>
- Meredith, N. P., Horne, R. B., Kersten, T., Fraser, B. J., & Grew, R. S. (2014). Global morphology and spectral properties of ionic waves derived from CRRES observations. *Journal of Geophysical Research: Space Physics*, *119*, 5328–5342. <https://doi.org/10.1002/2014JA020064>
- Meredith, N. P., Thorne, R. M., Horne, R. B., Summers, D., Fraser, B. J., & Anderson, R. R. (2003). Statistical analysis of relativistic electron energies for cyclotron resonance with ionic waves observed on CRRES. *Journal of Geophysical Research: Space Physics*, *108*. <https://doi.org/10.1029/2002JA009700>
- Min, K., Lee, J., Keika, K., & Li, W. (2012). Global distribution of ionic waves derived from themis observations. *Journal of Geophysical Research: Space Physics*, *117*. <https://doi.org/10.1029/2012JA017515>

- Morley, S. K., Brito, T. V., & Welling, D. T. (2018). Measures of model performance based on the log accuracy ratio. *Space Weather*, *16*, 69–88. <https://doi.org/10.1002/2017SW001669>
- Ni, B., Cao, X., Zou, Z., Zhou, C., Gu, X., Bortnik, J., et al. (2015). Resonant scattering of outer zone relativistic electrons by multi-band emic waves and resultant electron loss time scales. *Journal of Geophysical Research: Space Physics*, *120*, 7357–7373. <https://doi.org/10.1002/2015JA021466>
- Olsen, R. C., Chappell, C. R., Gallagher, D. L., Green, J. L., & Gunnert, D. A. (1985). The hidden ion population: Revisited. *Journal of Geophysical Research*, *90*, 12121. <https://doi.org/10.1029/ja090ia12p12121>
- Olson, J. V., & Lee, L. C. (1983). Pc1 wave generation by sudden impulses. *Planetary and Space Science*, *31*, 295–302.
- Olson, W. P., & Pfizter, K. A. (1977). *Magnetospheric magnetic field modeling annual scientific report*. Retrieved from <https://www.osti.gov/biblio/7212748https://www.osti.gov/servlets/purl/7212748>
- Ozhogin, P., Tu, J., Song, P., & Reinisch, B. W. (2012). Field-aligned distribution of the plasmaspheric electron density: An empirical model derived from the image rpi measurements. *Journal of Geophysical Research: Space Physics*, *117*. <https://doi.org/10.1029/2011JA017330>
- Pinto, V. A., Mourenas, D., Bortnik, J., Zhang, X. J., Artemyev, A. V., Moya, P. S., & Lyons, L. R. (2019). Decay of ultrarelativistic remnant belt electrons through scattering by plasmaspheric hiss. *Journal of Geophysical Research: Space Physics*, *124*, 5222–5233. <https://doi.org/10.1029/2019JA026509>
- Qin, M., Hudson, M., Li, Z., Millan, R., Shen, X., Shprits, Y., et al. (2019). Investigating loss of relativistic electrons associated with emic waves at low L values on 22 June 2015. *Journal of Geophysical Research: Space Physics*, *124*, 4022–4036. <https://doi.org/10.1029/2018JA025726>
- Reeves, G. D., Chen, Y., Cunningham, G. S., Friedel, R. W., Henderson, M. G., Jordanova, V. K., et al. (2012). Dynamic radiation environment assimilation model: DREAM. *Space Weather*, *10*. <https://doi.org/10.1029/2011SW000729>
- Ross, J. P. J., Glauert, S. A., Horne, R. B., Watt, C. E., Meredith, N. P., & Woodfield, E. E. (2020). A new approach to constructing models of electron diffusion by emic waves in the radiation belts. *Geophysical Research Letters*, *47*. <https://doi.org/10.1029/2020GL088976>
- Saikin, A. A., Zhang, J. C., Allen, R. C., Smith, C. W., Kistler, L. M., Spence, H. E., et al. (2015). The occurrence and wave properties of H⁺, He⁺, and O⁺-band emic waves observed by the Van Allen probes. *Journal of Geophysical Research: Space Physics*, *120*, 7477–7492. <https://doi.org/10.1002/2015JA021358>
- Saikin, A. A., Zhang, J. C., Smith, C. W., Spence, H. E., Torbert, R. B., & Kletzing, C. A. (2016). The dependence on geomagnetic conditions and solar wind dynamic pressure of the spatial distributions of emic waves observed by the Van Allen probes. *Journal of Geophysical Research - A: Space Physics*, *121*, 4362–4377. <https://doi.org/10.1002/2016JA022523>
- Schulz, M., & Lanzerotti, L. J. (1974). *Particle diffusion in the radiation belts* (Vol. 7). Springer Berlin Heidelberg. <https://doi.org/10.1007/978-3-642-65675-0>
- Shabansky, V. P. (1971). Some processes in the magnetosphere. *Space Science Reviews*, *12*, 299–418. <https://doi.org/10.1007/BF00165511>
- Sheeley, B. W., Moldwin, M. B., Rassoul, H. K., & Anderson, R. R. (2001). An empirical plasmasphere and trough density model: CRRES observations. *Journal of Geophysical Research: Space Physics*, *106*, 25631–25641. <https://doi.org/10.1029/2000ja000286>
- Shprits, Y. Y., Drozdov, A. Y., Spasojevic, M., Kellerman, A. C., Usanova, M. E., Engebretson, M. J., et al. (2016). Wave-induced loss of ultra-relativistic electrons in the Van Allen radiation belts. *Nature Communications*, *9*. <https://doi.org/10.1038/ncomms12883>
- Shprits, Y. Y., Horne, R. B., Kellerman, A. C., & Drozdov, A. Y. (2018). The dynamics of Van Allen belts revisited. *Nature Physics*, *14*, 102–103. <https://doi.org/10.1038/nphys435010.1038/nphys4350>
- Shprits, Y. Y., Subbotin, D., Drozdov, A., Usanova, M. E., Kellerman, A., Orlova, K., et al. (2013). Unusual stable trapping of the ultrarelativistic electrons in the Van Allen radiation belts. *Nature Physics*, *9*, 699–703. <https://doi.org/10.1038/nphys2760>
- Shprits, Y. Y., Subbotin, D., & Ni, B. (2009). Evolution of electron fluxes in the outer radiation belt computed with the verb code. *Journal of Geophysical Research: Space Physics*, *114*. <https://doi.org/10.1029/2008JA013784>
- Summers, D., Ni, B., & Meredith, N. P. (2007). Timescales for radiation belt electron acceleration and loss due to resonant wave-particle interactions: 2. Evaluation for vlf chorus, elf hiss, and electromagnetic ion cyclotron waves. *Journal of Geophysical Research: Space Physics*, *112*. <https://doi.org/10.1029/2006JA011993>
- Summers, D., & Thorne, R. M. (2003). Relativistic electron pitch-angle scattering by electromagnetic ion cyclotron waves during geomagnetic storm. *Journal of Geophysical Research: Space Physics*, *108*. <https://doi.org/10.1029/2002JA009489>
- Teng, S., Li, W., Tao, X., Ma, Q., Wu, Y., Capannolo, L., et al. (2019). Generation and characteristics of unusual high frequency emic waves. *Geophysical Research Letters*, *46*, 14230–14238. <https://doi.org/10.1029/2019GL085220>
- Thompson, R. L., Watt, C. E. J., & Williams, P. D. (2020). Accounting for variability in UFL wave radial diffusion models. *Journal of Geophysical Research: Space Physics*, *125*.
- Thorne, R. M., & Kennel, C. F. (1971). Relativistic electron precipitation during magnetic storm main phase. *Journal of Geophysical Research*, *76*, 4446–4453. <https://doi.org/10.1029/ja076i019p04446>
- Thorne, R. M., Li, W., Ni, B., Ma, Q., Bortnik, J., Baker, D. N., et al. (2013). Evolution and slow decay of an unusual narrow ring of relativistic electrons near L 3.2 following the September 2012 magnetic storm. *Geophysical Research Letters*, *40*, 3507–3511. <https://doi.org/10.1002/grl.50627>
- Tsurutani, B. T., & Smith, E. J. (1974). Postmidnight chorus: A substorm phenomenon. *Journal of Geophysical Research*, *79*(1), 118–127.
- Tsurutani, B. T., & Smith, E. J. (1977). Two types of magnetospheric elf chorus and their substorm dependences. *Journal of Geophysical Research*, *82*, 5112–5128. <https://doi.org/10.1029/ja082i032p05112>
- Usanova, M. E., Drozdov, A., Orlova, K., Mann, I. R., Shprits, Y., Robertson, M. T., et al. (2014). Effect of emic waves on relativistic and ultra-relativistic electron populations: Ground-based and Van Allen probes observations. *Geophysical Research Letters*, *41*, 1375–1381. <https://doi.org/10.1002/2013GL059024>
- Usanova, M. E., Mann, I. R., Bortnik, J., Shao, L., & Angelopoulos, V. (2012). Themis observations of electromagnetic ion cyclotron wave occurrence: Dependence on AE, SYMH, and solar wind dynamic pressure. *Journal of Geophysical Research: Space Physics*, *117*. <https://doi.org/10.1029/2012JA018049>
- Wang, D., & Shprits, Y. Y. (2019). On how high-latitude chorus waves tip the balance between acceleration and loss of relativistic electrons. *Geophysical Research Letters*, *46*, 7945–7954. <https://doi.org/10.1029/2019GL082681>
- Wang, D., Yuan, Z., Yu, X., Deng, X., Zhou, M., Huang, S., et al. (2015). Statistical characteristics of emic waves: Van Allen probe observations. *Journal of Geophysical Research: Space Physics*, *120*, 4400–4408. <https://doi.org/10.1002/2015JA021089>
- Wang, D., Yuan, Z., Yu, X., Huang, S., Deng, X., Zhou, M., & Li, H. (2016). Geomagnetic storms and emic waves: Van Allen probe observations. *Journal of Geophysical Research: Space Physics*, *121*, 6444–6457. <https://doi.org/10.1002/2015JA022318>
- Watt, C. E., Allison, H. J., Meredith, N. P., Thompson, R. L., Bentley, S. N., Rae, I. J., et al. (2019). Variability of quasilinear diffusion coefficients for plasmaspheric hiss. *Journal of Geophysical Research: Space Physics*, *124*, 8488–8506. <https://doi.org/10.1029/2018JA026401>

- Watt, C. E., Allison, H. J., Thompson, R. L., Bentley, S. N., Meredith, N. P., Glauert, S. A., et al. (2021). *The implications of temporal variability in wave-particle interactions in Earth's radiation belts* (Vol. 48). Blackwell Publishing Ltd. <https://doi.org/10.1029/2020GL089962>
- Zhang, X. J., Li, W., Thorne, R. M., Angelopoulos, V., Bortnik, J., Kletzing, C. A., et al. (2016). Statistical distribution of emic wave spectra: Observations from Van Allen probes. *Geophysical Research Letters*, 43(12), 348355–348412. <https://doi.org/10.1002/2016GL071158>